An intercomparison of bulk aerodynamic algorithms used over sea ice with data from the SHEBA experiment

SHORT TITLE: COMPARING SEA ICE ALGORITHMS WITH DATA

Michael A. Brunke[1], Mingyu Zhou[1,2], Xubin Zeng[1], and Edgar L Andreas[3]
[1] *Institute of Atmospheric Physics, The University of Arizona, Tucson, Arizona, USA*
[2] *National Research Center for Marine Environmental Forecasts, Beijing, China*
[3] *U.S. Army Cold Regions Research and Engineering Laboratory, Hanover, New Hampshire, USA*

Submitted to *JGR-Oceans*, 2 February 2005; Revised, 28 October 2005

INDEX TERMS: 0750 Cryosphere: Sea ice, 3349 Atmospheric processes: Polar meteorology, 3394 Atmospheric processes: Instruments and techniques, 4540 Oceanography: Physical: Ice mechanics and air/sea/ice exchange processes, 9315 Geographic location: Arctic region

KEYWORDS: air-sea-ice interaction, surface turbulent fluxes, bulk aerodynamic algorithms, annual cycle, diurnal cycle, regimes, roughness length, Arctic, SHEBA

Abstract

The presence of sea ice fundamentally changes the energy and momentum exchange between the ocean and the atmosphere in the Arctic. Thus, an accurate representation of the surface turbulent fluxes in climate models is a necessity. An intercomparison of bulk aerodynamic algorithms that calculate surface turbulent fluxes in four climate and numerical weather prediction models is undertaken using data from the Surface Heat Budget of the Arctic Ocean (SHEBA) field experiment, which occurred on the ice in the Beaufort and Chukchi Seas north of Alaska from October 1997 to October 1998. Algorithm deficiencies include the consistently higher wind stresses produced by the Arctic Regional Climate System Model (ARCSyM) algorithm; the lower sensible heat fluxes under stable conditions by the algorithms in ARCSyM, the National Center for Environmental Prediction's Global Forecasting System (GFS) model, and the European Center for Medium-Range Weather Forecasts (ECMWF) model; and the lower wind stresses by the National Center for Atmospheric Research's Community Climate System Model (CCSM) algorithm under stable conditions.

Unlike the constants used in most of the four model algorithms, the roughness lengths for momentum can be fitted by an exponential function with parameters that account for the seasonality in the roughness length. The roughness lengths for heat, z_{ot}, can be considered a constant (e.g., that used in CCSM, 0.5 mm), similar to what was found by *Andreas et al.* [2004]. When these roughness lengths were implemented into the CCSM and ECMWF algorithms, they produced slightly better wind stresses and sensible heat fluxes most of the time.

1. Introduction

The polar regions are a very important part of the global climate, as they are a heat sink for tropical energy. An integral component of the polar system is sea ice. Its presence modulates the exchange of energy between the atmosphere and the ocean. Sea ice also affects climate more generally through the ice-snow albedo feedback mechanism [*Curry et al.*, 1995] and via oceanic feedbacks involving ice growth and melt as well as the freshwater balance at the ice-ocean interface [*Stocker et al.*, 2001]. Several global models have demonstrated that, under increased-CO_2 scenarios, warming is greatest in the Arctic, enhanced by the retreat and thinning of the sea ice there [*Randall et al.*, 1998; *Houghton et al.*, 1990]. These models also showed large differences in the magnitude of the warming in this region [*Houghton et al.*, 1990, *Gates et al.*, 1996]. Furthermore, some models are even problematic in their control simulations in this region. For instance, version 2 of the National Center for Atmospheric Research (NCAR) Community Climate System Model (CCSM) is too warm by 8 K in the polar regions and simulates sea ice that is too thin in the Arctic [*Kiehl and Gent*, 2004].

Part of these differences could be due to differences in the parameterization of the surface energy balance. Small changes in this balance have been shown to effect model ice thickness [*Bitz and Lipscomb*, 1999]. This surface energy balance,

$$R_{\mathrm{SW}} + R_{\mathrm{LW}} + H_s + H_l + G + H_m = 0\,, \tag{1}$$

includes R_{SW} and R_{LW}, the net shortwave and longwave radiative fluxes at the surface, respectively; G, the conductive heat flux from the ice/snow interior; H_m, the heat flux used to melt ice in summer; and the turbulent fluxes of heat (sensible heat flux) H_s and moisture (latent heat flux) H_l, respectively. In this paper, upward (or downward) turbulent (H_s and H_l) fluxes are

defined to be positive (or negative), while the signs of the other terms are defined in the individual figure captions.

In numerical weather prediction and climate models, the turbulent heat fluxes and the turbulent flux of momentum (or wind stress, τ) are calculated using bulk surface turbulent flux algorithms. These algorithms generally employ Monin-Obukhov similarity theory to determine the turbulent fluxes from bulk variables of the surface and the first atmospheric model layer, such that

$$H_s = \rho_a c_p C_t U(\theta_s - \theta_a), \tag{2}$$

$$H_l = \rho_a L_s C_q U(q_s - q_a), \text{ and} \tag{3}$$

$$\tau = \rho_a C_m U^2 \ . \tag{4}$$

Here ρ_a is the density of air; c_p is the heat capacity of air at constant pressure; L_s is the latent heat of sublimation; U is the wind speed at the first model layer; θ_s and θ_a are the potential temperature at the surface and at the first model layer, respectively; q_s and q_a are the specific humidities at the surface and at the first model layer, respectively; and C_t, C_q, and C_m are the turbulent exchange coefficients for heat, moisture, and momentum, respectively.

The exchange coefficients are a function of the aerodynamic roughness lengths (z_{ot}, z_{oq}, and z_{om} for temperature, moisture, and momentum, respectively). For sea ice, the characteristic aerodynamic roughness lengths in models are usually considered to be constant and equal to each other. For example, in the CCSM all three roughness lengths are 0.5 mm. It is known, however, that the roughness length of sea ice varies according to the type and age of the ice [e.g., *Overland*, 1985; *Guest and Davidson*, 1991]. Also if there is snow on the ice, it can cause the momentum roughness to vary as the wind moves the snow around [e.g., *Andreas and Claffey*, 1995]. The motion of the sea ice can also cause surface inhomogeneities that affect the

aggregated roughness length of a model grid box. The ice could separate, creating leads of open water that have a different roughness length than the surrounding ice. Pressure ridges formed when ice floes come together also change the roughness as compared to undeformed ice. In summer, the ice partially melts, forming melt ponds. Leads are also more frequent in summer. These open-water areas create vertical surfaces at their edges that contribute to an increased momentum roughness [*Andreas et al.*, 2003, 2005b].

Another complication in determining surface turbulent fluxes over sea ice in polar regions is that the atmospheric boundary layer is mostly stably stratified. If the boundary layer is very stable, the surface layer, i.e, the bottom 10% of the total boundary layer, is usually isolated from the turbulence generated above by wind shear. Periodically, this turbulence can burst downwards into the surface layer as the Richardson number *Ri* is reduced below a critical value [*Businger*, 1973]. Breaking atmospheric gravity waves also enhance shear-generated turbulence in the surface layer [e.g., *Finnigan et al.*, 1984]. Just how much these contribute to the exchange coefficients is still largely unknown. Furthermore, measurements of exchange coefficients in the stable boundary layer are relatively rare.

These uncertainties in the physical processes at the atmosphere-ice interface were part of the motivation behind the experiment to study the Surface Heat Budget of the Arctic Ocean (SHEBA). The highlight of SHEBA was a yearlong field experiment from 2 October 1997 to 11 October 1998 centered around an ice camp that drifted with the pack ice in the Arctic Ocean [*Uttal et al.*, 2002]. Measurements during this campaign included eddy-correlation wind stresses, sensible heat fluxes, and latent heat fluxes at several sites. Here, these measurements will be compared to the turbulent fluxes calculated by the algorithms used by four climate and weather prediction models: the CCSM version 2, the European Centre for Medium-Range

Weather Forecasts (ECMWF) model, the Arctic Regional Climate System Model (ARCSyM), and the National Center for Environmental Prediction (NCEP) Global Forecasting System (GFS) model.

First, these algorithms are described in Section 2. Section 3 describes the SHEBA data used in this study, with the annual cycle of the observed data described in Section 4. Then, the results of the intercomparison are presented in Section 5. Some of the intercomparison results are further discussed in Section 6. Finally, conclusions are presented in Section 7.

2. Bulk aerodynamic algorithms

In general form, the exchange coefficients (C_t, C_q, and C_m) in equations (2)-(4) are

$$C_t = \frac{k^2}{\left[\ln\left(\frac{z}{z_{\mathrm{om}}}\right) - \psi_m\right]\left[\ln\left(\frac{z}{z_{\mathrm{ot}}}\right) - \psi_t\right]}, \tag{5}$$

$$C_q = \frac{k^2}{\left[\ln\left(\frac{z}{z_{\mathrm{om}}}\right) - \psi_m\right]\left[\ln\left(\frac{z}{z_{\mathrm{oq}}}\right) - \psi_t\right]}, \text{ and} \tag{6}$$

$$C_m = \frac{k^2}{\left[\ln\left(\frac{z}{z_{\mathrm{om}}}\right) - \psi_m\right]^2} \tag{7}$$

where k is the von Kármán constant (0.4) and z is the height of the first model layer. The terms ψ_m and ψ_t represent the effects of stability and are usually a function of the stability parameter $\zeta = z / L$ with L being the Obukhov length,

$$L = \frac{u_*^2 \theta_v}{kg\theta_{v*}} \tag{7a}$$

[*Garratt*, 1992]. The term u_* is the friction velocity, θ_{v*} is the scaling parameter for virtual potential temperature = $\left(\overline{w'\theta_v'}\right)\Big/u_*$ (w' and θ_v' are turbulent fluctuations in vertical velocity and virtual potential temperature, and the overbar denotes a time average), g is the acceleration of gravity, and θ_v is the layer-averaged virtual temperature.

Several studies have described how turbulent flux algorithms over the ocean differ in terms of how they parameterize the exchange coefficients and the roughness lengths [e.g., *Blanc,* 1985; *Zeng et al.*, 1998; *Brunke et al.*, 2002, 2003; *Chang and Grossman*, 1999]. The same is generally true for flux parameterizations over sea ice except that, because of the uncertainty as to what the roughness lengths over sea ice are, most models consistently equate the roughness lengths to the same constant. Of the four model algorithms that are compared in this study, three equate the roughness lengths to the same constant (0.1 mm in GFS, 0.5 mm in CCSM, and 1 mm in ECMWF). These three also parameterize ψ_m and ψ_t as functions of ζ as previously described in *Zeng et al.* [1998] and *Brunke et al.* [2002]. Their formulations for ψ_m and ψ_t (not shown) are fairly close for unstable conditions ($\zeta < 0$) but diverge under stable conditions ($\zeta > 0$)

The fourth model, ARCSyM, differentiates between snow-covered and bare ice. For snow depths less than 5 cm, z_{om} is 60 mm but is reduced to 40 mm for greater snow depths. Furthermore, in the parameterization of the momentum exchange coefficient, ARCSyM calculates C_m from the neutral coefficient, $C_{mn} = k^2 \big/ \left[\ln\left(z/z_{\mathrm{om}}\right)\right]^2$, such that

$$C_m = C_{mn} f_m \tag{8}$$

where f_m varies with the bulk Richardson number in the surface layer, Ri_b:

$$f_m = \frac{1 - 40Ri_b}{1 + C_{m1}Ri_b^{1/2}} \text{ where } C_{m1} = 296C_{mn}\left(\frac{z}{z_{\mathrm{om}}}\right)^{1/2} \text{ for } Ri_b < 0, \text{ and} \tag{9}$$

$$f_m = \frac{1}{(1+20Ri_b)^2} \text{ for } Ri_b \geq 0. \quad (10)$$

The exchange coefficient for moisture in ARCSyM is calculated thusly:

$$C_q = 1.0022\times10^{-3} + 8.22\times10^{-5}\Delta T + 2.66\times10^{-4}U \quad (11)$$

where ΔT is the surface-air temperature difference and U is the wind speed. The exchange coefficient for heat C_t is taken as 94% of C_q.

3. Turbulent heat flux and bulk measurements during SHEBA

The SHEBA field experiment began on 2 October 1997. The activities during the experiment were centered around the Canadian Coast Guard ship *Des Groseilliers*, which was frozen into the ice at 75°N, 142°W in the Beaufort Sea north of Alaska. The ice camp that was established around the ship drifted with the ice around the Beaufort Gyre, ending up at 80°N, 166°W at the end of the experiment on 11 October 1998 [*Uttal et al.*, 2002; *Persson et al.*, 2002].

Turbulent flux measurements were made on a 20-m tower in the main camp and at four remote NCAR portable automated mesonet (PAM) [*Militzer et al.*, 1995] stations. The tower was set up in an area 280 to 350 m from the ship. The location of the tower relative to the ship varied as the ice floe rotated and sheared apart [*Persson et al.*, 2002], but the tower generally had an upwind fetch over undisturbed ice that was 240° wide. Three of the PAM stations, named Atlanta, Baltimore, and Florida, were continuously operational during the yearlong experiment (http://www.atd.ucar.edu/rtf/projects/sheba), and data from these are used in this study. Florida was about 100 m from the 20-m tower, while Atlanta and Baltimore ranged from 1 to 10 km distant.

On the 20-m tower, slow measurements of temperature and relative humidity (RH) were made at the six levels given in Table 1 by Väisälä HMP235 T/RH probes equipped with R. M.

Young aspirated shields [*Andreas et al.*, 2002]. These measurements were made every 5 s. At the same levels, fast measurements of wind velocities and temperature were made by Applied Technologies, Inc. (ATI) sonic anemometer/thermometers sampling at 10 Hz. An Ophir fast hygrometer was located at only one level (8.1 m) to measure humidity at a rate of 20 Hz. On two nearby masts, radiometric measurements of longwave (LW) and shortwave (SW) radiation were made by two sets of Eppley pyrgeometers and pyranometers, respectively, in which one was pointed up and another down. Also nearby was a downward pointing Barnes PRT-5 precision radiation thermometer to measure surface temperature. Surface temperatures were also determined from the Eppley pyrgeometers. The Barnes temperatures were used from 24 May to 28 June, and the Eppley temperatures were used during the rest of the year. The heights of the radiometric measurements and their sampling rates are also given in Table 1. The accuracy of the tower instruments have been discussed in *Persson et al.* [2002].

At the PAM stations, slow measurements of temperature and RH were made by Väisälä Hummiter 50Y sensors equipped with NCAR mechanically aspirated radiation shields. These sensors were generally placed at a height of 1.5 to 2 m. As on the main tower, the PAM stations used sonic anemometer/thermometers to make fast measurements of the wind vector and the temperature. Each station, however, had only one sonic, and none had any fast humidity measurements. Both ATI and Gill Instruments R2 Solent sonics were used on the PAM stations. The ATI sonics sampled at 10 Hz and were at a height between 2.25 and 3.25 m; the Gills sampled at 21 Hz and were typically at a height of 3.5 m. Early in the experiment, both types of sonics frequently suffered riming that degraded the velocity and temperature measurements. Heating added to the transducer heads finally cured this problem in mid-January 1998.

As in the main camp, the PAM sites also had upward-looking and downward-looking pyrgeometers and pyranometers. The upward-looking radiometers, especially, also suffered from riming until powerful heaters and blowers were installed by April 1998. Here, we ignore the PAM covariance fluxes measured by the sonic anemometers and the surface temperatures derived from the pyrgeometer measurements before these instruments began operating reliably. The accuracy of the instruments at the PAM stations is described at http://www.atd.ucar.edu/rtf/projects/sheba.

From the sonic anemometer measurements, the covariances of vertical velocity fluctuations w' with the fluctuations of the horizontal wind components with respect to the direction of the hourly mean wind direction (u_s') and of the virtual temperature (T_v'), i.e., $\overline{u_s'w'}$ and $\overline{T_v'w'}$, can be computed. The covariance of $\overline{q'w'}$ was similarly computed at the tower using the fast hygrometer measurements of q'. The turbulent fluxes (wind stress and latent and sensible heat fluxes) are related to these covariances thusly:

$$\tau = -\rho_a\left(\overline{u_s'w'}\right) \tag{12}$$

$$H_s = \rho_a c_p\left[\overline{T_v'w'} - 0.51\overline{q'w'}\right], \text{ and} \tag{13}$$

$$H_l = \rho_a L_s \overline{q'w'}\,. \tag{14}$$

A minor correction for the Webb effect [*Webb et al.*, 1980] was made to H_l which was measured only at the tower. The data recovery for $\overline{q'w'}$ at the tower is much less than for $\overline{T_v'w'}$ so that bulk estimates of H_l were used to calculate H_s when $\overline{q'w'}$ was not available. This latter term is very small and can be neglected. So, for the PAM stations, where there were no measurements of $\overline{q'w'}$, we simply use $H_s = \rho_a c_p \overline{T_v'w'}$.

The tower data were quality controlled based on objective and subjective criteria including validity limits on the streamwise and vertical velocity variances. Hourly PAM data were also flagged as bad if the percentage of non-missing measurements within the hour was less than 99.5% or if the heaters were on sometime during the hour. Also, fluxes were ignored if the tower or boom structure was upwind from the sonic anemometers. This screening leaves a total of 13 138 hourly data points for wind stress, 14 040 for sensible heat flux, and 3209 for latent heat flux.

4. The annual cycle during SHEBA

Figure 1 presents the annual cycle of various measurements made at the 20-m tower. The monthly mean wind speed at the tower does not vary much and is around 4 m s^{-1} (Figure 1a). Both surface and air temperatures are lowest in the winter (December, January, and February) with air temperatures warmer than surface temperatures by about 1°C (Figure 1b). After February, temperatures rise to summer levels of about 0°C from June through August [cf. *Andreas et al.*, 2002]. The air temperatures at SHEBA were comparable to those from other experiments in the Arctic except during the spring (March and April) when they were 3°-8°C higher [*Persson et al.*, 2002].

Shortwave radiation was negligible early in the experiment (Figure 1c). Beginning in March, shortwave radiation increases to its maximum value in June of about 270 W m^{-2} for downward radiation. Upward shortwave radiation is smaller, with a maximum in June of about 200 W m^{-2}. The monthly mean albedo computed as the ratio between monthly upward shortwave radiation and downward shortwave radiation for months with shortwave fluxes greater than 25 W m^{-2} varies from 0.56 in July 1998 to 0.87 in April 1998. Longwave radiation (Figure 1d) is lowest in the winter and highest in the summer, as would be expected from the

temperatures. Upward longwave radiation is higher than downward radiation by 11 W m^{-2} in September 1998 to 35 W m^{-2} in February 1998.

Figure 2 presents all of the observed fluxes including the net radiative (R_{SW} and R_{LW}) and turbulent fluxes (H_s, which was measured at all sites; and H_l, which was measured only at the tower). Also shown are the residual in equation (1) calculated from the above observed fluxes: $-G - H_m$ at the tower and $-H_l - G - H_m$ at the PAM stations. Throughout the year, the sensible and latent heat fluxes are very small. Thus, the energy balance is dominated by the net shortwave flux during the summer and the net longwave flux during the winter.

Figure 3 shows the monthly mean turbulent fluxes combined, with positive fluxes being upward. There is a minimum in the sensible heat fluxes from all of the sites combined in the winter ranging from about -4 to -10 W m^{-2}, and it becomes slightly positive in summer (Figure 3a). As with wind speed, wind stress from all of the sites combined is fairly constant (Figure 3b). Latent heat flux from the 20-m tower only is near-zero in winter and increases only to about 2 W m^{-2} in summer (Figure 3c).

5. Intercomparison of model fluxes with SHEBA data

5.1. Monthly fluxes

Figure 3 also shows the turbulent fluxes computed from the four model algorithms described in Section 2 with data from all of the sites combined. These fluxes have been derived by the algorithms that have been isolated from their models in which the observed values from the SHEBA experiment of wind speed, air temperature, and surface temperature were input into these algorithms. The algorithms produce sensible heat fluxes (Figure 3a) that are within one standard deviation of the observations throughout the year, even though the algorithm fluxes are slightly lower than observed in May, July, and August. Wind stresses (Figure 3b) from CCSM,

ECMWF, and GFS are close to observed, while ARCSyM's wind stresses are badly overestimated. The latent heat fluxes computed using all algorithms are close to observed values except in June, when they are significantly overestimated (Figure 3c). Of course, latent heat flux is the least reliable of the turbulent fluxes from SHEBA [*Persson et al.*, 2002].

5.2. Diurnal cycle

The observed diurnal cycle is compared to the algorithm results for each of the four seasons at the 20-m tower in Figures 4-7. During September to November (SON), observed hourly mean sensible heat flux (Figure 4a) is generally slightly negative throughout the day. Algorithm sensible heat fluxes are within one standard deviation of the observed means. Observed latent heat flux (Figure 4b) is also fairly constant near zero throughout the day; the algorithm means are generally within one standard deviation of the observed means. All algorithms, however, produce a maximum in latent heat flux at 10:00 local time that is not observed.

In December to February (DJF), observed sensible heat flux (Figure 4c) is even more negative than in SON. Again, the algorithm fluxes are within one standard deviation of the observed means. Observed latent heat flux (Figure 4d) is practically zero throughout the day with very small standard deviations. Three of the algorithms (CCSM, ECMWF, and GFS) generally produce latent heat fluxes that are slightly lower than one standard deviation from the observed means.

From March to May (MAM), the observed sensible heat flux cycle (Figure 4e) is more pronounced, with an amplitude of about 14 W m^{-2}. The algorithms produce a much smaller diurnal amplitude with sensible heat fluxes with much lower than the observed fluxes from 8:00 to14:00 local time. The observed latent heat flux cycle (Figure 4f) is also more pronounced in

MAM with a nearly 3 W m^{-2} amplitude. While the algorithms produce a smaller amplitude in latent heat flux, their fluxes are all within the observed interquartile ranges.

Finally, during July to August (JJA), the observed sensible heat flux diurnal cycle (Figure 4g) is quite a bit lower (only about 5 W m^{-2}) than in MAM. The nighttime fluxes from the algorithms are simulated fairly well, but their fluxes remain fairly constant throughout the day. Observed latent heat flux (Figure 4h) also has a smaller diurnal cycle in JJA (below 2 W m^{-2}) than in MAM. Fluxes from CCSM, ECMWF, and ARCSyM generally are above a standard deviation throughout most of the day.

The pronouncement or lack of the diurnal cycles in the observed sensible and latent heat fluxes in each of the seasons can be partially explained by the net radiative fluxes, since, from equation (1), the sum of the heat fluxes including the conductive heat flux and the melt energy flux is equal to the sum of the net radiative fluxes. So, the hourly mean net shortwave and longwave radiative fluxes are presented in Figures 5 and 6. The net longwave fluxes are fairly constant throughout the day in every season except MAM (Figure 5c) when there is a slight maximum at 12:00 local time. The diurnal cycle in net shortwave flux is small in SON (Figure 6a) and almost non-existent in DJF (Figure 6b). In contrast, the diurnal cycles in MAM and JJA (Figure 6c and d) are much larger, with the largest amplitude in JJA. Even with the large diurnal cycle in shortwave flux in JJA, the nonexistent cycle in longwave flux and reduced cycles in latent and sensible heat fluxes must mean that the conductive heat flux and, especially, the melt energy flux are more important during this season (e.g., Figure 2).

The algorithms, however, respond only to the bulk variables provided to them. In this study, these are the observed wind speed, air temperature, and surface temperature. Thus, the diurnal cycles in the algorithm sensible and latent heat fluxes seen here would reflect the diurnal

cycles in these observations. Observed surface and air temperatures are nearly constant throughout the year even in MAM and JJA (not shown) resulting in the small diurnal cycles in the algorithm sensible heat fluxes seen in Figures 4e and g. In fact, the observed surface and air temperatures in JJA are almost identical; the algorithms thus produce near-zero fluxes throughout the day. The diurnal cycles in humidity are more pronounced in MAM and JJA (not shown) than in the rest of the year, resulting in the larger diurnal cycles in latent heat flux produced by the algorithms during these two seasons. The diurnal cycle of humidity is the highest in JJA, which results in the larger diurnal cycle in algorithm latent heat flux in this season compared to MAM. The maximum latent heat fluxes at 10:00 local time in SON are produced because the median air humidity at that hour dips below that at the surface. Thus, more situations in which the algorithms will produce upward latent heat fluxes are being sampled at this hour. Clearly, these results show that the turbulent heat fluxes in the real world respond to more than just what is going on in the atmospheric boundary layer as is parameterized by these model algorithms.

Both observed and algorithm wind stresses are fairly constant throughout the day during all seasons, so only the hourly means from the whole year at the 20-m tower are shown in Figure 7. The wind stresses produced by CCSM, ECMWF, and GFS are within one standard deviation of the observed means, while ARCSyM's stresses are substantially higher than observed.

5.3. Stability regimes

Figure 8 shows the algorithm and observed fluxes, binned as a function of 2.5-m bulk Richardson number Ri_b [cf. *Grachev et al.*, 2003]:

$$Ri_b = \frac{2.5g\left(\theta_v(2.5) - \theta_{vs}\right)}{\theta_v(2.5)U(2.5)^2} \tag{15}$$

Previous studies have shown several regimes for stable conditions [e.g., *Mahrt et al.*, 1998; *Mahrt*, 1999; *Grachev et al.*, 2005]: a weakly stable, a transitional, and a very stable regime. Downward sensible heat flux increases to a maximum in the weakly stable regime and then decreases in the transitional regime to a very small negative value in the very stable regime [*Mahrt et al.*, 1998; *Jordan et al.*, 1999].

Figure 8a is consistent with this picture: the magnitude of observed sensible heat flux from all of the sites combined generally increases with increasing Ri_b to a minimum at $Ri_b \approx 0.05$. For $0.05 < Ri_b < 0.25$, observed sensible heat flux decreases in magnitude to very small values at $Ri_b \geq 0.25$, the widely held critical Richardson number for the termination of turbulence in the stable boundary layer [*Chimonas*, 1999]. The sensible heat fluxes from CCSM and ECMWF are relatively close to observed. Still, the sensible heat fluxes from ECMWF are lower than observed interquartile ranges, i.e., the difference between the 25th and 75th percentiles, while those from ARCSyM and GFS are even lower still.

For unstable conditions ($Ri_b < 0$), observed sensible heat fluxes are positive. All algorithms produce sensible heat fluxes that are slightly lower than observed but generally within observed interquartile ranges (Figure 8a).

For wind stress from all of the sites combined (Figure 8b), there is a maximum in the observations of nearly 0.05 N m^{-2} for near-neutral conditions ($-0.05 < Ri_b < 0.05$). Observed wind stress is one order of magnitude smaller under more stable conditions due to turbulence damping by the stratification and under more unstable conditions usually associated with weak winds. All algorithms reproduce the peak for near-neutral conditions. However, ARCSyM overestimates wind stress under unstable and weakly stable conditions. Under very stable

conditions, CCSM underestimates its wind stresses, while ARCSyM's wind stresses reduce to a range within the observed interquartile ranges.

Observed latent heat fluxes from the 20-m tower only (Figure 8c) are positive for unstable conditions ($Ri_b < 0$), having a maximum at Ri_b = -0.05 of about 1.8 W m^{-2}, and near zero for stable conditions ($Ri_b > 0$). Three algorithms (CCSM, ECMWF, and GFS) produce negative fluxes under stable conditions. This pattern is similar to how these algorithms behave for sensible heat fluxes under stable conditions. ARCSyM, on the other hand, sets latent heat flux to a constant 0 W m^{-2} when the air-surface humidity difference is less than zero; it thus prohibits downward latent heat fluxes despite observations to the contrary (namely, frequent riming).

5.4. Comparison at the various levels of the 20-m tower under various stability regimes

The above comparisons were made only at one level. As was stated in Section 3, sensible heat and momentum flux measurements at the 20-m tower were made at five other levels as well. Figures 9-10 compare the observed profiles of sensible heat fluxes and wind stresses, respectively, and those produced by the algorithms for four stability regimes: unstable, weakly stable, transitional, and very stable regimes.

From these figures, how the observed fluxes behave as a function of height can be seen and compared with previous results. In the unstable regime (Figure 9a and e), observed sensible heat flux is a maximum at level 2 in both winter (October to March) and summer (April to September). In winter, the median sensible heat fluxes from the upper levels above level 2 are still about 1 W m^{-2} higher than at level 1, whereas the medians at levels 4 and 5b in summer are about 1 W m^{-2} lower than at level 1. This contradicts *Howell and Sun*'s [1999] finding that sensible heat flux should be independent of height under unstable conditions. On the other hand, the observed median sensible heat fluxes at the levels above level 1 are all higher than at the

lowest level under stable conditions (Figure 9b-d). In fact, in the weakly stable and transitional regimes (Figure 9b and c), the magnitude of sensible heat flux generally decreases monotonically in magnitude with increasing height, consistent with *Howell and Sun* [1999, Figure 4]. In summer, however, the median sensible heat fluxes are slightly lower at the upper levels in the weakly stable and transitional regimes (Figure 9f and g). Only under very stable conditions (Figure 9h) are the upper level sensible heat fluxes slightly higher than at level 1.

Observed wind stress under unstable conditions in both winter and summer (Figure 10a and e) is essentially independent of height, consistent with *Howell and Sun* [1999]. In the weakly stable regime (Figure10b and f), there is a small increase in wind stress with height, particularly in winter. In the transitional regime (Figure 10c and g), observed wind stress is highest at level 1 in both seasons. In winter, wind stress is independent of height above the lowest level; whereas in summer, the transitional regime shows another maximum at level 4. Under very stable conditions in winter (Figure 10d), wind stress is nearly independent of height from level 4 and below and decreases to a minimum at level 5a. In summer, wind stress steadily decreases with height under very stable conditions (Figure 10h). The dependence of wind stress in the transitional and very stable conditions seen here contradict *Howell and Sun*'s [1999] finding of independence of momentum flux under all conditions.

Model algorithms calculate surface fluxes based on the mean bulk variables in the lowest atmospheric layer which has a depth that varies from around 20 m in numerical weather prediction models to well above 20 m in climate models (e.g., around 60 m in CCSM). Furthermore, the same algorithm is used when the model vertical resolution is increased with the increase in computing power. Therefore, it is useful to evaluate the vertical profiles of the fluxes produced by the algorithms. What would be preferable for the algorithms is for them to produce

vertical profiles that fall within the uncertainty of the observed near-surface fluxes, i.e., the interquartile ranges of the observed level 1 fluxes.

For sensible heat flux, the profiles from CCSM, ECMWF, and GFS are essentially constant with height in the unstable regime (Figure 9a and e) in both summer and winter. ARCSyM's sensible heat fluxes increase with height during both winter and summer. All algorithms produce sensible heat fluxes at all levels that are within the observed interquartile range at level 1.

Under weakly stable conditions in winter (Figure 9b), the vertical profiles from CCSM, ECMWF, and GFS are again almost constant, while ARCSyM now produces sensible heat fluxes that decrease with height. In fact, its median flux at the highest level (5a) is lower than the observed interquartile range at level 1. In summer, however, all algorithms have nearly constant profiles with height within the observed interquartile range at level 1, so all algorithms produce sensible heat fluxes above level 1 close to what they would produce near-surface.

In the transitional and very stable regimes in both winter and summer (Figure 9c-d and g-h), GFS and ECMWF have nearly constant or slightly decreasing profiles that are outside of even the observed interquartile range at level 1, except in the winter transitional regime (Figure 9c) ARCSyM has a profile in both seasons that decreases with height so that its fluxes from the highest level are much lower than at level 1. CCSM produces sensible heat fluxes in the transitional regime (Figure 9c and g) that increase with increasing height, while they are almost constant under very stable conditions (Figure 9d and h).

As with sensible heat flux, CCSM, ECMWF, and GFS have nearly constant wind stress profiles at all levels in the unstable and weakly stable regimes in both winter and summer

(Figures 10a-b and e-f). ARCSyM's profiles are much higher than the level 1 observations and decrease with height with the rate of decrease becoming less with height.

In the transitional regime in winter (Figure 10c), ARCSyM continues to have a profile that decreases with height, but its wind stress at level 5a is within the observed interquartile range at level 1. ECMWF and GFS now produce wind stresses that increase with height. ECMWF's wind stresses are within the observed interquartile range at level 1 at all levels, while GFS produces wind stresses above the observed level 1 interquartile range above level 2. CCSM's wind stress is maximum at level 2, but its wind stresses are within the observed level 1 interquartile range at all levels.

In the summertime transitional regime (Figure 10g), all algorithms except GFS produce profiles with a minimum wind stress at some height. GFS's wind stress increases with height at all levels, and the rate of increase is higher at upper levels. CCSM's wind stresses are within the observed level 1 interquartile range as in the wintertime transitional regime (Figure 10c).

Under very stable conditions (Figure 10d and h), CCSM's wind stresses increase slightly with height. In winter (Figure 10d), CCSM's wind stresses are slightly below or within the observed interquartile range at level 1, while, in summer (Figure 10h), its wind stresses are well below the observed level 1 interquartile range at all levels. In winter, ECMWF and GFS have increasing wind stress profiles with height, and ARCSyM has wind stresses that slightly decrease with height. ECMWF's and ARCSyM's wind stresses are within the observed level 1 interquartile range at all levels, while GFS produces wind stresses that are above the level 1 interquartile range at levels at or above level 3. In summer, ECMWF, ARCSyM, and GFS have minimum wind stresses. ARCSyM's wind stresses are well below the observed level 1 interquartile range at all levels. ECMWF wind stresses increase at level 4 to just below the

observed 25th percentile at level 1, and GFS' wind stresses are well within the observed level 1 interquartile range at level 4.

5.5. Wind speed regimes

Figures 11-12 show the median turbulent fluxes for 0.5-m s^{-1} wind speed bins. At each site, zero sensible heat flux is within the interquartile ranges of observed fluxes in most bins (Figure 11). At the tower (Figure 11a), model algorithm sensible heat fluxes agree well with observed fluxes for $U < 10$ m s^{-1}. For higher wind speeds, the sensible heat fluxes produced by all of the model algorithms are generally too low being close to zero. At the PAM sites (Figures 11b-d), all algorithms diverge from observations to highly negative values starting at around $U =$ 4 m s^{-1}, and, at Baltimore and Florida (Figure 11c and d), the algorithms sensible heat fluxes that have a maximum in magnitude around $U = 8$ m s^{-1}. Many of the turbulent fluxes measured early at these sites were removed due to the frequent riming of the instruments. A comparison of the median surface and air temperatures (not shown) for these higher wind speed bins reveals that the temperatures being sampled at these sites were colder.

For all of the sites combined, observed wind stress increases with wind speed (Figure 12a). At 0.75 m s^{-1}, wind stress is on the order of 10^{-3} N m^{-2}; at 12.25 m s^{-1}, it is about 0.3 to 0.4 N m^{-2}. The wind stresses are generally well reproduced by CCSM, ECMWF, and GFS; while ARCSyM greatly overestimates wind stress for all wind speeds.

Finally, observed latent heat fluxes at the 20-m tower (Figure 12b) generally increase from near-zero at low wind speeds to 1-2 W m^{-2} at high wind speeds with large variations, particularly at higher wind speeds. These variations are likely due to the large measurement errors, which are on the order of or larger than the median values as shown by the interquartile ranges in Figure 12b. At low wind speeds, the model algorithms generally underestimate the

latent heat flux, with three of the four algorithms (CCSM, ECMWF, and GFS) producing negative latent heat fluxes. At higher wind speeds, the algorithm fluxes also vary but are within the observed interquartile ranges.

6. Discussion of results

6.1. Sensitivity tests

Admittedly, the comparison of these four model algorithms using point measurements as input is somewhat questionable, since these algorithms were developed for global models in which an average value over a grid box is supposed to be used as input. However, some of the large differences between the algorithms are due to the differences between the algorithm parameterizations such as differences in roughness lengths or in the stability terms, ψ_m and ψ_t. Of particular note are the consistently higher wind stresses produced by ARCSyM (e.g., Figures 3, 7-8, and 12), the lower wind stresses by CCSM under stable conditions (e.g., Figure 8b), and the higher magnitude sensible heat fluxes by GFS and ARCSyM in the transitional and very stable regimes (e.g., Figure 8a). For instance, ARCSyM's roughness lengths for momentum, 40 mm or 60 mm, are much higher than those used in the other algorithms and are not compatible with observations. This is the primary reason for the higher wind stresses produced by this algorithm.

Under stable conditions, the calculation of turbulent fluxes becomes sensitive to the parameterization of the exchange coefficients, which are affected by the roughness lengths and the stability terms used. ARCSyM's exchange coefficients for heat and moisture are not derived from Monin-Obukhov similarity theory but instead from an empirical relationship. Also, GFS's stability terms are empirical profile relations not standardly used. Finally, while the use of -5ζ for ψ_t produces sensible heat fluxes very close to observed in CCSM under stable conditions, its

use for ψ_m underestimates wind stress. Previous work has shown that ψ_m is better represented under stable conditions by other formulations such as that of *Holtslag and De Bruin* [1988] as is used in ECMWF [e.g., *Jordan et al.*, 1999; *Andreas*, 2002]. However, equating ψ_t under stable conditions with the ψ_m from *Holtslag and De Bruin* [1988], as is done in ECMWF, produces sensible heat fluxes that are slightly low for $Ri_b > 0.1$.

To test how much these differences in the parameterizations in these four algorithms contribute to the differences in the fluxes between the algorithms and observed, we performed four experiments for ARCSyM, three experiments for GFS, and two experiments each for CCSM and ECMWF. These experiments involved slight changes to each of the parameterizations. The resulting sensible heat fluxes and wind stresses from the experimental versions of the algorithms are compared to the observations and to the original versions as functions of Ri_b for all of the sites combined in Figure 13.

For ARCSyM, the first experiment (hereafter referred to as ARCSyM-1) involved lowering the roughness lengths to more reasonable values. The values chosen were that used in CCSM for bare ice and in GFS for snow-covered ice. Also changed was how C_t was found by using Monin-Obukhov similarity theory similar to what is used for C_m in equations (8)-(10), except that $C_t = C_{tn} f_m / 0.74$ and $C_{t1} = 212\ C_{tn}\ (z / z_{ot})^{1/2}$. This substantially improves the sensible heat fluxes (Figure 13a) for $Ri_b > 0.1$, which are now within the observed interquartile ranges. The wind stresses (Figure 13b) under near-neutral and unstable conditions are also greatly improved, but those for $Ri_b > 0.2$ are now much lower than observed interquartile ranges.

In the second experiment (hereafter referred to as ARCSyM-2), the Richardson-number-based formulation was replaced by a standard one based on ζ. The stability terms used under stable conditions in this case were -5ζ, as is used in CCSM. As would be expected from

previous results from CCSM (e.g., Figure 8), ARCSyM-2 produces near-zero sensible heat fluxes (Figure 13a) for $Ri_b > 0.1$, but its wind stresses (Figure 13b) are lower than the observed interquartile ranges for $Ri_b > 0.4$.

A third experimental version (hereafter referred to as ARCSyM-3) in which the *Holtslag and De Bruin* [1988] stability terms from ECMWF are used instead under stable conditions increases the wind stresses (Figure 13b) to within the observed interquartile ranges for every bin but decreases the sensible heat fluxes (Figure 13a) to just below observed interquartile ranges for $Ri_b > 0.1$.

In the final experiment (hereafter referred to as ARCSyM-4), the *Holtslag and De Bruin* [1988] formulation is used for ψ_m and -5ζ is used for ψ_t. ARCSyM-4 produces sensible heat fluxes (Figure 13a) similar to those from ARCSyM-3, but its wind stresses (Figure 13b) are slightly higher than those from ARCSyM-3. This is still much improved upon the original formulation as the sensible heat fluxes under very stable conditions and the wind stresses under near-neutral and unstable conditions are much closer to observed than before.

Similar experiments were also undertaken to replace GFS's empirical profile relations under stable conditions. In the first experiment (hereafter referred to as GFS-1), the algorithm's stability terms for stable conditions were changed to those used in CCSM (i.e., -5ζ for both momentum and heat). For the second experiment (hereafter referred to as GFS-2), the GFS stability terms under stable conditions were replaced by those used in ECMWF (i.e., *Holtslag and De Bruin's* [1988]). In the final experiment, the *Holtslag and De Bruin* [1988] function was used for ψ_m and -5ζ was used for ψ_t.

As would be expected by previous results, GFS-1 produces near-zero sensible heat fluxes (Figure 13c) that are very close to observed for $Ri_b > 0.2$ while producing wind stresses (Figure

13d) smaller than observed interquartile ranges. GFS-2 produces better wind stresses (Figure 13d) under very stable conditions, but its sensible heat fluxes (Figure 13c) are slightly below observed interquartile ranges. Both wind stress and sensible heat flux (Figure 13c,d) are slightly improved by GFS-3. While there is a sacrifice made to the wind stresses under very stable conditions with GFS-3, the wind stresses are still generally within the observed interquartile ranges, and the sensible heat fluxes are much closer to observed under very stable conditions than before. So, this is again a big improvement to GFS.

CCSM and ECMWF could also be improved by using the *Holtslag and De Bruin* [1988] function for ψ_m and -5ζ for ψ_t. Figure 13e and f show CCSM's two experimental versions, one in which *Holtslag and De Bruin*'s [1988] function was used for both ψ_m and ψ_t (CCSM-1) and the other in which only ψ_m was replaced by the *Holtslag and De Bruin* [1988] function (CCSM-2). Figure 13g and h show ECMWF's two experimental versions, one in which -5ζ was used for both ψ_m and ψ_t (ECMWF-1) and the other in which only ψ_t was replaced by -5ζ, along with the original versions of the respective algorithms. While there is a slight sacrifice in the sensible heat fluxes in CCSM under very stable conditions ($Ri_b > 0.25$), CCSM-2 produces much better wind stresses in this regime. There is also a slight improvement in the wind stresses produced by ECMWF-2, which are now within the observed interquartile ranges for all bins.

6.2. Observed roughness lengths during the SHEBA experiment

To evaluate the validity of the roughness lengths used by the model algorithms compared here, the roughness lengths were derived from the observed turbulent fluxes at the 20-m tower and the PAM stations during the SHEBA experiment using equations (2)-(7) and (12)-(14). The stability terms ψ_m and ψ_t in equations (5)-(7) are taken from *Zeng et al.* [1998].

Figure 14 shows the median observed momentum roughness lengths for 2°C bins of surface temperature as well as the roughness lengths used in each of the model algorithms compared here indicated by the thin horizontal lines. This temperature dependence is explored here because the nature of the ice changes from snow-covered ice at the coldest temperatures to melting snow and eventually bare ice. Such a change in the ice also produces a change in the surface albedo, and several global models parameterize albedo as a function of surface temperature [e.g. *Curry et al.*, 2001]. A change in the roughness length can be seen at the 20-m tower and Florida (Figure 14a,d). The roughness lengths at temperatures above about -2°C are higher than those for colder temperatures. The roughness lengths at the tower increase again for temperatures less than -23°C. At Baltimore (Figure 14c), the roughness length is rather constant at about the CCSM roughness length. At Atlanta (Figure 14b), the roughness length is also quite constant at the CCSM value down to about -14°C but then decreases for colder surface temperatures. These differences in the nature of the roughness lengths among these sites are due to the various ice characteristics for which these sites were chosen.

Also shown in Figure 14 are the median momentum roughness lengths produced by the *Andreas et al.* [2004] algorithm [cf. *Andreas et al.*, 2005a], which is

$$z_{\mathrm{om}} = \frac{0.135\nu}{u_*} + \frac{0.035u_*^2}{g}\left\{1 + A\exp\left[-\left(\frac{u_* - 0.18}{0.10}\right)^2\right]\right\}. \qquad (16)$$

where ν is the kinematic viscosity of air and A is a coefficient that is tuned for a particular location. For SHEBA, $A = 1$. For the most part, the *Andreas et al.* [2004] roughness lengths are generally within the interquartile ranges of the observed roughness lengths except between -7°C and -23°C at the 20-m tower. This is not surprising, since the algorithm has been tuned to the observed roughness lengths here.

Figure 15 presents the median roughness lengths for temperature, z_{ot}, for surface temperature bins for all of the sites combined. Unlike the roughness lengths for momentum, the roughness lengths for heat generally fluctuate around the value used in GFS, ECMWF, and CCSM. Also shown are the median roughness lengths for temperature based on *Andreas's* [1987] formulation, which depends on z_{om} and the roughness Reynolds number, $\mathrm{Re}_* = u_* z_{om} / \nu$. *Andreas's* [1987] roughness lengths for heat are generally within the observed interquartile ranges.

Figure 16 shows the median roughness lengths for temperature for bins of friction velocity u_* for all of the sites combined. As with the surface temperature bins, the median roughness lengths for heat have large fluctuations. The roughness lengths predicted by *Andreas [1987]* are typically within an order of magnitude of the observed roughness lengths, as was found in *Andreas et al.* [2004]. For practical purposes, z_{ot} could well be considered a constant at 0.5 mm as is used in CCSM.

Figure 14 suggests that there might be a slight seasonality to the momentum roughness lengths. The year can be divided into two seasons aerodynamically speaking: winter when there is dry snow on the ice, and summer during the rest of the year. During the SHEBA experiment, aerodynamic summer is defined as 15 May 1998 through 14 September 1998 [*Andreas et al.*, 2003]. The observed median roughness lengths for momentum for bins of u_* are shown separately for the aerodynamic winter (Figure 17) and summer (Figure 18).

During the aerodynamic winter, the lowest roughness lengths are at very low friction velocities, but these results may be unreliable due to measurement uncertainties at such low u_*. For $u_* \geq$ about 0.05 m s^{-1}, roughness lengths tend to increase more or less exponentially. Also shown in Figure 17 is a fit of an exponential form that is simpler than equation (16):

$$z_{\mathrm{om}}\ (\mathrm{m}) = \begin{cases} 7\times10^{-4} - 6.5\times10^{-4}\, e^{-4(u_*-0.05)} & \text{for } u_* \geq 0.05\ \mathrm{m\ s^{-1}} \\ 5\times10^{-5} & \text{for } u_* < 0.05\ \mathrm{m\ s^{-1}} \end{cases}. \tag{17}$$

The roughness lengths produced by this formulation generally fall within the interquartile ranges of the observed z_{om}, except for a few bins at the 20-m tower and at Florida. This formulation's bias is -6.7×10^{-4} m, and its standard deviation of the difference between the modeled and observed roughness lengths is 4.2×10^{-3} m. The roughness length parameterization from *Andreas et al.* [2004] is also shown in Fig. 17. It is also very consistent with the observed roughness lengths with a bias of -7.1×10^{-4} m and standard deviation of the difference of 4.2×10^{-3} m.

During the aerodynamic summer, the winter snow melts away leaving bare ice. Eventually, melt ponds and leads form, creating vertical surfaces around their edges that increase the momentum roughness length [*Andreas et al.*, 2003, 2005b]. Figure 18 shows that z_{om} is generally larger in the aerodynamic summer than in winter. The roughness length still increases exponentially with u_* at a higher rate than in winter. Also shown in Figure 18 are the median roughness lengths for a formulation of z_{om} similar to that used in Figure 17 during winter:

$$z_{\mathrm{om}}\ (\mathrm{m}) = \begin{cases} \rho\left[7\times10^{-4} - 6.5\times10^{-4}\, e^{-\gamma(u_*-0.05)}\right] & \text{for } u_* \geq 0.05\ \mathrm{m\ s^{-1}} \\ 5\times10^{-5}\,\rho & \text{for } u_* < 0.05\ \mathrm{m\ s^{-1}} \end{cases}. \tag{18}$$

where γ and ρ linearly increase from surface temperatures of -2°C to 0°C such that

$$\gamma = \begin{cases} 3T_s + 10 & \text{for } -2°\mathrm{C} < T_s \leq 0°\mathrm{C} \\ 4 & \text{for } T_s \leq -2°\mathrm{C} \end{cases} \tag{19}$$

and

$$\rho = \begin{cases} 1.4 + 0.2T_s & \text{for } -2°\mathrm{C} < T_s \leq 0°\mathrm{C} \\ 1 & \text{for } T_s \leq -2°\mathrm{C} \end{cases}. \tag{20}$$

This formulation's bias in summer is -6.9×10^{-4} m and the standard deviation of the difference between its roughness lengths and those observed is 3.4×10^{-3} m.

Implementation of equation (18) in model algorithms involves several iterations in the computation of surface fluxes. Because the CCSM and ECMWF algorithms already include iterations in their codes, it is straightforward to test (18) in them. Table 2 lists the median differences of sensible heat flux and wind stress between the original CCSM and ECMWF algorithms and those when z_{om} is replaced by equation (18) and z_{ot} is 0.5 mm (which doesn't change in CCSM). For sensible heat flux, both algorithms produce slightly lower fluxes with the new roughness lengths under unstable conditions ($Ri_b \leq 0$), where these algorithms originally produced too high fluxes (Figure 8).

In the stable regimes, sensible heat flux produced with the new roughness lengths are higher (less negative), with the largest increase in the transitional regime ($0.05 < Ri_b \leq 0.25$). This would lead to a slight improvement to both algorithms' sensible heat fluxes in the weakly stable ($0 < Ri_b \leq 0.05$) and transitional ($0.05 < Ri_b \leq 0.25$) regimes and in ECMWF under very stable conditions ($Ri_b > 0.25$).

For wind stress, both algorithms produce smaller values using equation (18). The magnitude of the median differences is higher in the unstable ($Ri_b \leq 0$) and weakly stable regimes ($0 < Ri_b \leq 0.05$). The median difference decreases in magnitude with increasing stability. For CCSM, the lower wind stresses in the very stable regime ($Ri_b > 0.25$) wouldn't be detrimental because the amount of decrease is two orders of magnitude smaller than the magnitude of the original stresses (Figure 8, Table 2). So, the change in roughness length proposed here would slightly improve the algorithms under most conditions.

The response to the change in roughness lengths differs between the two algorithms; ECMWF is more sensitive to this change. Part of this difference is due to other differences between the algorithms such as the stability functions used. This difference, particularly for sensible heat flux, is also due to the fact that z_{ot} is lowered in ECMWF but is not changed in CCSM.

7. Conclusions

Data collected during the Surface Heat Budget of the Arctic Ocean (SHEBA) field experiment were used to compare and evaluate the bulk aerodynamic algorithms used to calculate surface turbulent fluxes over sea ice in four climate and weather models: the National Center for Atmospheric Research's Community Climate System Model (CCSM), the European Centre for Medium-Range Weather Forecasts (ECMWF) model, the Arctic Regional Climate System Model (ARCSyM), and the National Center for Environmental Prediction's Global Forecasting System (GFS) model. The data come from the five levels of the 20-m tower at the ice camp and from three of the four portable mesonet (PAM) stations set up around the ice camp. Some of the surface fluxes produced by these algorithms show significant differences in the annual and diurnal cycles. For instance in summer, the sensible heat fluxes from all of the algorithms are lower than observed. Also, the latent heat fluxes from all of the algorithms are much higher than observed in June and August.

Some of these algorithms are problematic under certain conditions. ECMWF, ARCSyM, and GFS produce sensible heat fluxes under stable conditions that are lower than observed interquartile ranges, particularly for the transitional ($0.05 < Ri_b \leq 0.25$) and very stable ($Ri_b > 0.25$) regimes. CCSM's sensible heat fluxes are quite good under very stable conditions ($Ri_b > 0.25$), but its wind stresses in this regime are quite a bit smaller than the observed interquartile

ranges. Also, ARCSyM's wind stresses are too high for unstable and near-neutral conditions, mostly due to its large roughness lengths for momentum. This algorithm's higher wind stresses would have obvious direct effects on ice motion in this model and indirect effects on ice thickness, extent, and export due to the difference in ice motion.

Sensitivity tests were performed to show just how much of these differences are due to differences in the choices for roughness length and functions used to account for the effects of stability in these algorithms. The underestimation in sensible heat fluxes in ECMWF and GFS under stable conditions was shown to be due to the terms that they use to account for the effects of stability. Similarly in ARCSyM, the empirically-derived exchange coefficient for heat, C_t, (see Section 2) was shown to have an effect on its sensible heat fluxes. The -5ζ used for ψ_t in CCSM reproduces sensible heat flux quite well under very stable conditions ($Ri_b > 0.25$), its use for ψ_m as well leads to a poor reproduction of wind stress under these conditions.

The atmosphere was stable most of the time during SHEBA. During the winter, observed sensible heat fluxes at the 20-m tower increase (or decrease in magnitude) with height in all but the most stable regime ($Ri_b > 0.25$, Figure 9d), as seen in previous results [cf. *Howell and Sun*, 1999]; while in summer, they are nearly constant with height, which contradicts previous results from *Howell and Sun* [1999]. Three of the four algorithms (ECMWF, ARCSyM, and GFS) have vertical profiles of sensible heat flux that are generally outside of the observed interquartile ranges at level 1 in the transitional ($0.05 < Ri_b \leq 0.25$, Figure 9c and g) and very stable ($Ri_b > 0.25$, Figure 9d and h) regimes. Also, ARCSyM's wind stresses are much higher than the observed level 1 interquartile ranges unstable ($Ri_b \leq 0$, 10a and e) and weakly stable ($0 < Ri_b \leq 0.05$, 10b and f) conditions but decrease with increasing height. The other algorithms have

nearly constant wind stress profiles within the observed level 1 interquartile ranges in these regimes.

Observed roughness lengths for momentum and heat (z_{om} and z_{ot}, respectively) were calculated from the observed wind stresses and sensible heat fluxes at the tower and the PAM stations. There does not appear to be a dependence of z_{ot} on surface temperature or u_*; therefore, a constant z_{ot} (e.g., 0.5 mm, as is used in CCSM) could remain to be used in models, similar to what *Andreas et al.* [2004] found. Observed z_{om} is higher at surface temperatures warmer than about -2°C at the 20-m tower and the PAM station Florida, which was located in the vicinity of the tower. Observed z_{om} at all four sites also appear to be an exponential function of the friction velocity u_*. The roughness lengths calculated using the *Andreas et al.* [2004] scheme are a fairly good fit to the observed z_{om} in the aerodynamic winter (before about mid-May and after about mid-September). An equally good but simpler fit that is applicable throughout the year is that of equations (18)-(20). These two suggestions for z_{om} and z_{ot} do have a small impact on the calculated wind stresses and sensible heat fluxes in CCSM and ECMWF but would possibly have a larger impact in another algorithm, e.g., ARCSyM, which had much larger roughness lengths than any of the other algorithms.

Acknowledgments. This work was supported by the NSF (ATM0301188) and NOAA (NA03NES4400013). Mingyu Zhou was also partially supported by the NSF of China (40233032). We thank Drs. H.-L. Pan, H. Juang, A. Beljaars, and J. Cassano for providing their algorithms and Dr. S. Lu for providing technical support on the GFS algorithm.

References

Andreas, E. L (1987), A theory for the scalar roughness and the scalar transfer coefficients over snow and sea ice, *Boundary-Layer Meteorol.*, *38*, 159-184.

Andreas, E. L (2002), Parameterizing scalar transfer over snow and ice: A review, *J. Hydrometeorol.*, *3*, 417–432.

Andreas, E. L, and K. J. Claffey (1995), Air-ice drag coefficients in the western Weddell Sea 1. Values deduced from profile measurements, *J. Geophys. Res.*, *100* (C3), 4821-4831.

Andreas, E. L, P. S. Guest, P. O. G. Persson, C. W. Fairall, T. W. Horst, R. E. Moritz, and S. R. Semmer (2002), Near-surface water vapor over polar sea ice is always near ice saturation, *J. Geophys. Res.*, *107* (C10), SHE 8-1, doi: 10.1029/2000JC000411.

Andreas, E. L, C. W. Fairall, A. A. Grachev, P. S. Guest, T. W. Horst, R. E. Jordan, and P. O. G. Persson (2003), Turbulent transfer coefficients and roughness lengths over sea ice: The SHEBA results, paper presented at 7th Conference on Polar Meteorology and Oceanography, Am. Meteorol. Soc., Hyannis, Mass.

Andreas, E. L, R. E. Jordan, P.S. Guest, P. O. G. Persson, A. A. Grachev, and C. W. Fairall (2004), Roughness lengths over snow, Preprint CD-ROM, paper presented at 18th Conference on Hydrology, Am. Meteorol. Soc., Seattle, Wash.

Andreas, E. L, R. E. Jordan, and A. P. Makshtas (2005a), Parameterizing turbulent exchange over sea ice: The Ice Station Weddell results, *Boundary-Layer Meteorol.*, *114*, 439–460.

Andreas, E. L, P. O. G. Persson, R. E. Jordan, T. W. Horst, P. S. Guest, A. A. Grachev, and C. W. Fairall (2005b), Parameterizing the turbulent surface fluxes over summer sea ice.

Preprint CD-ROM, paper presented at 8th Conference on Polar Meteorology and Oceanography, Am. Meteorol. Soc., San Diego, Calif.

Bitz, C. M., and W. H. Lipscomb (1999), An energy-conserving thermodynamic model of sea ice, *J. Geophys. Res.*, *104*, 15,669-15,677.

Blanc, T. V. (1985), Variation of bulk-derived surface flux, stability, and roughness results due to the use of different transfer coefficient schemes, *J. Phys. Oceanogr., 15*, 650–669.

Brunke, M. A., X. Zeng, and S. Anderson (2002), Uncertainties in sea surface turbulent flux algorithms and data sets, *J. Geophys. Res.*, *107* (C10), 3141, doi: 10.1029/2001JC000992.

Brunke, M. A., C. W. Fairall, X. Zeng, L. Eymard, J. A. Curry (2003), Which bulk aerodynamic algorithms are least problematic in computing ocean surface turbulent fluxes?, *J. Clim.*, *16*, 619-635.

Businger, J. A. (1973), Turbulent transfer in the atmospheric surface layer, in *Workshop on Micrometeorology*, edited by D. H. Haugen, Am. Meteorol. Soc., pp. 67-100.

Chang, H.-R., and R. L. Grossman (1999), Evaluation of bulk surface algorithms for light wind conditions using data from the Coupled Ocean-Atmosphere Response Experiment (COARE), *Q. J. R. Meteorol. Soc.*, *125*, 1551-1588.

Chimonas, G. (1999), Steps, waves and turbulence in the stably stratified boundary layer. *Boundary-Layer Meteorol.*, *90*, 397-421.

Curry, J. A., J. L. Schramm, E. E. Ebert (1995), Sea ice-albedo climate feedback mechanism, *J. Clim.*, *8*, 240-247.

Curry, J. A., J. L. Schramm, D. K. Perovich, and J. O. Pinto (2001), Application of SHEBA/FIRE data to evaluation of snow/ice albedo parameterization, *J. Geophys. Res.*, *106* (D14), 15,345-15,355.

Finnigan, J. J., F. Einaudi, and D. Fua (1984), The interaction between an internal gravity wave and turbulence in the stably-stratified nocturnal boundary layer, *J. Atmos. Sci.*, *41*, 2409-2436.

Garratt, J. R. (1992), *The Atmospheric Boundary Layer*, 316 pp., Cambridge Univ. Press, New York.

Gates, W. L., and Coauthors (1996), Climate models—Evaluation, in *Climate Change 1995*, edited by J. T. Houghton, L. G. Meira Filho, B. A. Callander, N. Harris, A. Kattenberg, and K. Maskell, pp. 233-284, Cambridge Univ. Press, New York.

Grachev, A. A., C. W. Fairall, P. O. G. Persson, E. L Andreas, P. S. Guest, and R. E. Jordan (2003), Turbulence decay in the stable Arctic boundary layer, Preprint CD-ROM, paper presented at 7th Conference on Polar Meteorology and Oceanography, Am. Meteorol. Soc., Hyannis, MA.

Grachev, A. A., C. W. Fairall, P. O. G. Persson, E. L Andreas, and P. S. Guest (2005), Stable boundary-layer scaling regimes: The SHEBA data, *Boundary-Layer Meteor.*, to appear.

Guest, P. S., and K. L. Davidson (1991), The aerodynamic roughness of different types of sea ice, *J. Geophys. Res.*, *96* (C3), 4709-4721.

Holtslag, A. A. M., and H. A. R. de Bruin (1988), Applied modeling of the nighttime surface energy balance over land, *J. Appl. Meteorol.*, *27*, 689-704.

Houghton, J. T., G. J. Jenkins, and J. J. Ephraums (Eds.) (1990), *Climate Change: The IPCC Scientific Assessment*, 364 pp., Cambridge Univ. Press, New York.

Howell, J. F., and J. Sun (1999), Surface-layer fluxes in stable conditions, *Boundary-Layer Meteorol.*, *90*, 495-520.

Jordan, R. E., E. L Andreas, and A. P. Makshtas (1999), The heat budget of snow-covered sea ice at North Pole 4, *J. Geophys. Res.*, *104*, 7785–7806.

Kiehl, J. T., and P. R. Gent (2004), The Community Climate System Model, version 2, *J. Clim.*, *17*, 3666-3682.

Mahrt, L., J. Sun,W. Blumen, T. Delany, and S. Oncley (1998), Nocturnal boundary-layer regimes, *Boundary-Layer Meteorol.*, *88*, 255-278.

Mahrt, L. (1999), Stratified atmospheric boundary layers, *Boundary-Layer Meteorol.*, *90*, 375-396.

Militzer, J. M., M. C. Michaelis, S. R. Semmer, K. S. Norris, T. W. Horst, S. P. Oncley, A. C. Delany, and F. V. Brock (1995), Development of the prototype PAM III/Flux-PAM surface meteorological station, paper presented at 9th Symposium on Meteorological Observations and Instrumentation, Am. Meteorol. Soc., Charlotte, N.C.

Overland, J. E. (1985), Atmospheric boundary layer structure and drag coefficients over sea ice, *J. Geophys. Res.*, *90*, 9029–9049.

Persson, P. O. G., C. W. Fairall, E. L. Andreas, P. S. Guest, and D. K. Perovich (2002), Measurements near the Atmospheric Surface Flux Group tower at SHEBA: Near-surface conditions and surface energy budget, *J. Geophys. Res.*, *107* (C10), 8045, doi: 10.1029/2000JC000705.

Randall, D. A., and Coauthors (1998), Status of and outlook for large-scale modeling of atmosphere-ice-ocean interactions in the Arctic, *Bull. Am. Meteorol. Soc.*, *79*, 197-219.

Stocker, T. F., and Coauthors (2001), Physical climate processes and feedbacks, in *IPCC Climate Change 2001: The Scientific Basis*, edited by J. T. Houghton and Co-editors, pp. 417-470, Cambridge University Press, New York.

Uttal, T., and Coauthors (2002), Surface Heat Budget of the Arctic Ocean, *Bull. Am. Meteorol. Soc.*, *83*, 255-275.

Webb, E. K., G. J. Pearman, and R. Leuning (1980), Correction of flux measurements for density effects due to heat and water vapor transport, *Q. J. R. Meteorol. Soc.*, *106*, 85-100.

Zeng, X., M. Zhao, and R. E. Dickinson (1998), Intercomparison of bulk aerodynamic algorithms for the computation of sea surface fluxes using TOGA COARE and TAO data, *J. Clim.*, *11*, 2628-2644.

Addresses

Michael A. Brunke and Xubin Zeng, Institute of Atmospheric Physics, The University of Arizona, Physics-Atmospheric Sciences Bldg., P.O. Box 210081, Tucson, AZ 85721-0081, USA. (brunke@atmo.arizona.edu; zeng@atmo.arizona.edu)

Mingyu Zhou, National Research Center for Marine Environmental Forecasts, 8 Dahuisi, Haidian District, Beijing 100081, People's Republic of China. (mingyuzhou@yahoo.com)

Edgar L Andreas, U.S. Army Cold Regions Research and Engineering Laboratory, 72 Lyme Road, Hanover, NH 03755-1290, USA. (eandreas@crrel.usace.army.mil)

Table 1. The instruments on and near the 20-m tower at SHEBA used in this study.[a]

Flux	Level	Mean height (m)	Sampling rate
Väisälä HMP 235 T/RH probes	1	2.2	0.2 Hz
	2	3.2	0.2 Hz
	3	5.1	0.2 Hz
	4	8.9	0.2 Hz
	5a	13.8	0.2 Hz
	5b	17.6	0.2 Hz
Applied Technologies Inc. (ATI) sonic anemometers	1	2.2	10 Hz
	2	3.2	10 Hz
	3	5.1	10 Hz
	4	8.9	10 Hz
	5a	13.8	10 Hz
	5b	17.6	10 Hz
Ophir fast hygrometer		8.1	20 Hz
Eppley pyrgeometers (4.0-50.0 μm wavelengths)		1.5-2.0	0.2 Hz
Eppley pyranometers (0.29-2.80 μm wavelengths)		1.5-2.0	0.2 Hz
Barnes PRT-5 (9.5-11.5 μm wavelengths)		1.0	0.2 Hz
Väisälä PTB 220B digital barometer		1.0	1 Hz

[a] Suffixes a and b denote winter and summer heights, respectively.

Table 2. The Median Differences of Sensible Heat Flux and Wind Stress Between the Original CCSM and ECMWF Algorithms and Those Using Equation (18) for z_{om} and 0.5 mm for z_{ot}

	CCSM		ECMWF	
Regime	Original Median	Median Difference	Original Median	Median Difference
	Sensible heat flux (W m^{-2})			
Unstable ($Ri_b \le 0$)	3.04	-0.08	3.26	-0.62
Weakly stable ($0 < Ri_b \le 0.05$)	-7.69	0.18	-8.10	1.55
Transitional ($0.05 < Ri_b \le 0.25$)	-2.78	1.14	-5.09	2.05
Very stable ($Ri_b > 0.25$)	-0.38	0.02	-1.32	0.37
	Wind stress (N m^{-2})			
Unstable ($Ri_b \le 0$)	0.038	-0.002	0.040	-0.008
Weakly stable ($0 < Ri_b \le 0.05$)	0.051	-0.003	0.054	-0.01
Transitional ($0.05 < Ri_b \le 0.25$)	0.002	-8.5×10^{-4}	0.003	-0.001
Very stable ($Ri_b > 0.25$)	8.3×10^{-5}	-6.2×10^{-6}	3.2×10^{-4}	-1.0×10^{-4}

Figure Captions

Figure 1. Monthly mean (a) wind speed, (b) surface and air temperatures, and downward and upward (c) shortwave (SW) and (d) longwave (LW) radiation (magnitude only) at the 20-m tower.

Figure 2. The energy budget at (a) the 20-m tower and the PAM stations (b) Atlanta, (c) Baltimore, and (d) Florida. At the tower, the net shortwave radiation (R_{SW}), net longwave radiation (R_{LW}), latent heat flux (H_l), sensible heat flux (H_s), and the sum of these, which is equal to $-G - H_l$ (only shown when all of the sum can be calculated), are shown. At the PAM stations, only R_{SW}, R_{LW}, $-H_s$, and the net sum of these, which is equal to $-H_l - G - H_m$, are shown, since latent heat flux was not measured at these sites. Positive fluxes are upward; negative fluxes are downward.

Figure 3. Monthly mean observed covariance (a) sensible heat (SH) fluxes, (b) wind stress, and (c) latent heat (LH) fluxes along with the algorithm-produced fluxes from CCSM, ECMWF, ARCSyM, and GFS for all of the four stations combined for (a,b) and for the 20-m tower for (c). The thin vertical lines represent one standard deviation about the mean.

Figure 4. Hourly mean observed covariance (a,c,e,g) sensible heat flux, (b,d,f,h) latent heat flux along with the algorithm-produced fluxes from CCSM, ECMWF, ARCSyM, and GFS at the 20-m tower in (a,b) September-October-November (SON), (c,d) December-January-February (DJF), (e,f) March-April-May (MAM), and (g,h) June-July-August (JJA). The thin vertical lines represent one standard deviation about the mean.

Figure 5. Hourly mean observed net longwave radiative fluxes at the 20-m tower in (a) SON, (b) DJF, (c) MAM, and (d) JJA. Positive fluxes are upward; negative fluxes are downward.

Figure 6. Same as in Figure 5 except for shortwave fluxes.

Figure 7. Hourly mean observed covariance wind stress along with the algorithm-produced fluxes from CCSM, ECMWF, ARCSyM, and GFS at the 20-m tower. The thin vertical lines represent one standard deviation about the mean.

Figure 8. Median observed covariance (a) sensible heat fluxes, (b) wind stress, and (c) latent heat flux and the algorithm-produced fluxes from CCSM, ECMWF, ARCSyM, and GFS as a function of the bulk Richardson number Ri_b at 2.5 m in 0.1 bins for all of the four stations combined for (a,b) and for the 20-m tower for (c). The thin vertical lines represent the interquartile range, i.e., the difference between the 25th and 75th percentiles.

Figure 9. Median observed covariance sensible heat fluxes and the algorithm-produced fluxes from CCSM, ECMWF, ARCSyM, and GFS at each level of the 20-m tower for (a)-(d) winter (October to March) and (e)-(h) summer (April to September) in the (a,e) unstable ($Ri_b \leq 0$); (b,f) weakly stable ($0 < Ri_b \leq 0.05$); (c,g) transitional ($0.05 < Ri_b \leq 0.25$); and (d,h) very stable ($Ri_b > 0.25$) regimes. The thin horizontal lines represent the interquartile range, i.e., the difference between the 25th and 75th percentiles, and the shaded box shows the observed interquartile range at level 1.

Figure 10. Same as in Figure 9 except for wind stress.

Figure 11. Median observed covariance sensible heat fluxes and the algorithm-produced fluxes from CCSM, ECMWF, ARCSyM, and GFS for 0.5 m s^{-1} bins of wind speed at 2.5 m at (a) the 20-m tower and the PAM stations (b) Atlanta, (c) Baltimore, and (d) Florida. The thin vertical lines represent the interquartile range, i.e., the difference between the 25th and 75th percentiles.

Figure 12. Median observed covariance (a) wind stress for all of the four stations combined and (b) latent heat fluxes at the 20-m tower and the algorithm-produced fluxes from CCSM, ECMWF, ARCSyM, and GFS for 0.5 m s^{-1} bins of wind speed at 2.5 m. The thin vertical lines represent the interquartile range, i.e., the difference between the 25th and 75th percentiles.

Figure 13. Median observed covariance (a,c,e,g) sensible heat fluxes and (b,d,f,h) wind stresses for all of the four stations combined. The thin vertical lines represent the interquartile range. Also plotted are the sensible heat fluxes calculated by (a,b) ARCSyM and its altered versions used in the sensitivity tests (ARCSyM-1, ARCSyM-2, ARCSyM-3, ARCSyM-4), GFS and its altered versions (GFS-1, GFS-2, GFS-3), CCSM and its altered versions (CCSM-1, CCSM-2), and ECMWF and its altered versions (ECMWF-1, ECMWF-2).

Figure 14. Median observed roughness lengths for momentum (z_{om}) for 2°C bins of surface temperature at (a) the 20-m tower and the PAM stations (b) Atlanta, (c) Baltimore, and (d) Florida. The thin vertical lines represent the interquartile range. Also shown are the roughness lengths from the *Andreas et al.* [2004] scheme as well as those used in ECMWF, CCSM, and GFS.

Figure 15. Median observed roughness lengths for heat (z_{ot}) for 2°C bins of surface temperature for all of the four stations combined. The thin vertical lines represent the interquartile range. Also shown are the roughness lengths from the *Andreas* [1987] scheme as well as those used in ECMWF, CCSM, and GFS.

Figure 16. Median observed z_{ot} for 0.02 m s^{-1} bins of friction velocity u_* for all of the four stations combined. The thin vertical lines represent the interquartile range. Also shown are

the roughness lengths from the *Andreas* [1987] scheme as well as those used in ECMWF, CCSM, and GFS.

Figure 17. Median observed z_{om} for 0.02 m s^{-1} bins of friction velocity u_* at (a) the 20-m tower and the PAM stations (b) Atlanta, (c) Baltimore, and (d) Florida during the winter aerodynamically speaking (before 15 May 1998 and after 14 September 1998). The thin vertical lines represent the interquartile range. Also shown are the median roughness lengths derived from equation (17) as well as those from the *Andreas et al.* [2004] scheme and those used in ECMWF, CCSM, and GFS.

Figure 18. Same as in Figure 17 except for aerodynamic summer. Also shown are the median roughness lengths from equations (18)-(20).

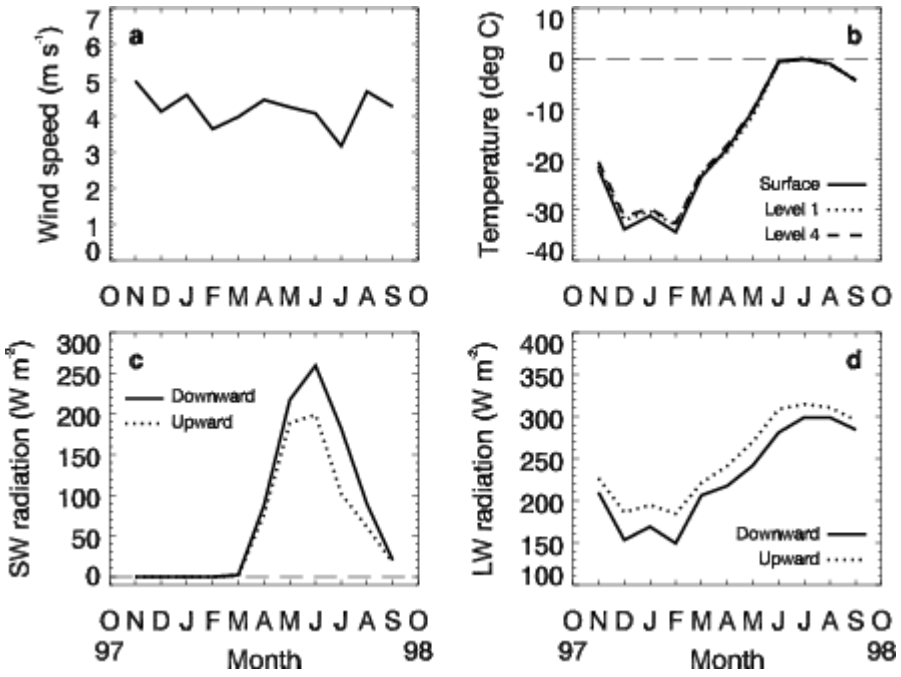

Figure 1. Monthly mean (a) wind speed, (b) surface and air temperatures, and downward and upward (c) shortwave (SW) and (d) longwave (LW) radiation (magnitude only) at the 20-m tower.

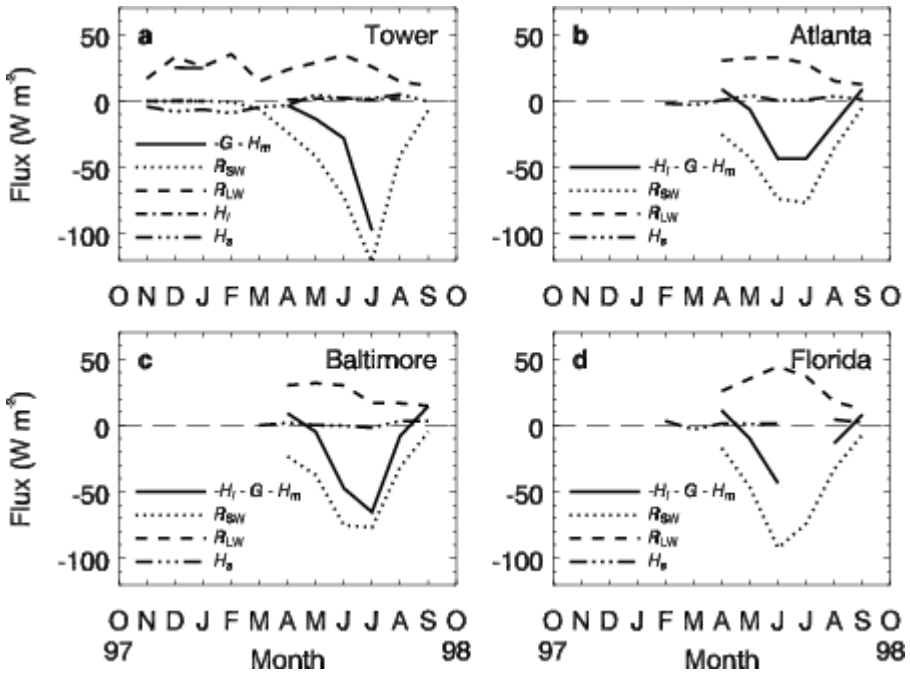

Figure 2. The energy budget at (a) the 20-m tower and the PAM stations (b) Atlanta, (c) Baltimore, and (d) Florida. At the tower, the net shortwave radiation (R_{SW}), net longwave radiation (R_{LW}), latent heat flux (H_l), sensible heat flux (H_s), and the sum of these, which is equal to $-G - H_l$ (only shown when all of the sum can be calculated), are shown. At the PAM stations, only R_{SW}, R_{LW}, $-H_s$, and the net sum of these, which is equal to $-H_l - G - H_m$, are shown, since latent heat flux was not measured at these sites. Positive fluxes are upward; negative fluxes are downward.

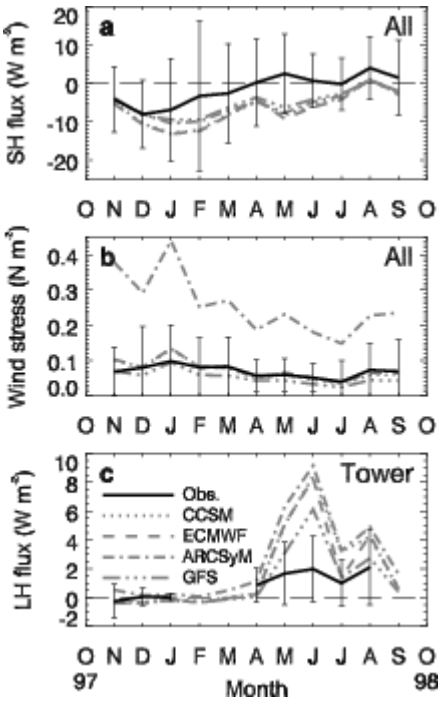

Figure 3. Monthly mean observed covariance (a) sensible heat (SH) fluxes, (b) wind stress, and (c) latent heat (LH) fluxes along with the algorithm-produced fluxes from CCSM, ECMWF, ARCSyM, and GFS for all of the four stations combined for (a,b) and for the 20-m tower for (c). The thin vertical lines represent one standard deviation about the mean.

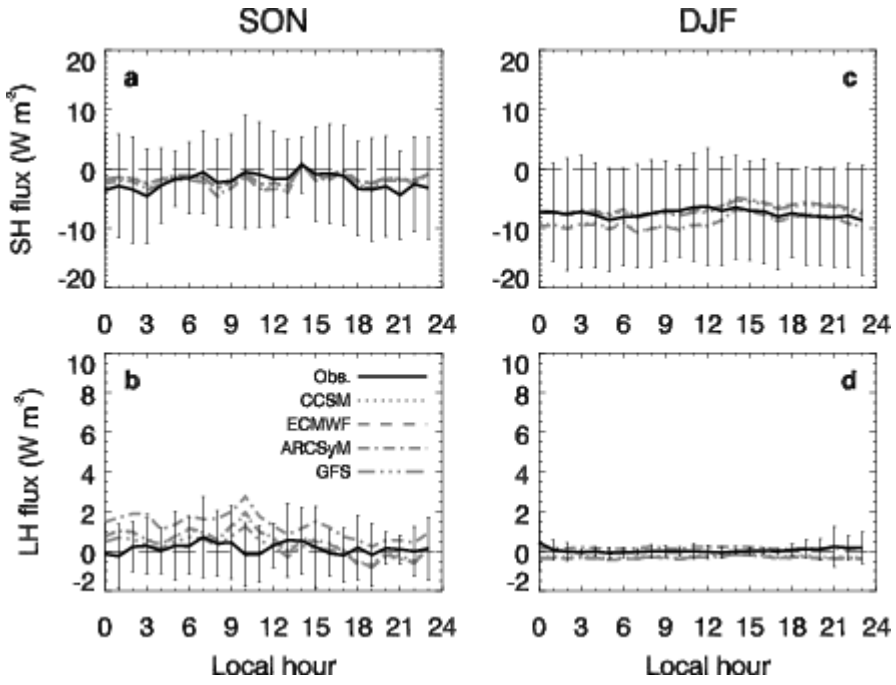

Figure 4. Hourly mean observed covariance (a,c,e,g) sensible heat flux, (b,d,f,h) latent heat flux along with the algorithm-produced fluxes from CCSM, ECMWF, ARCSyM, and GFS at the 20-m tower in (a,b) September-October-November (SON), (c,d) December-January-February (DJF), (e,f) March-April-May (MAM), and (g,h) June-July-August (JJA). The thin vertical lines represent one standard deviation about the mean.

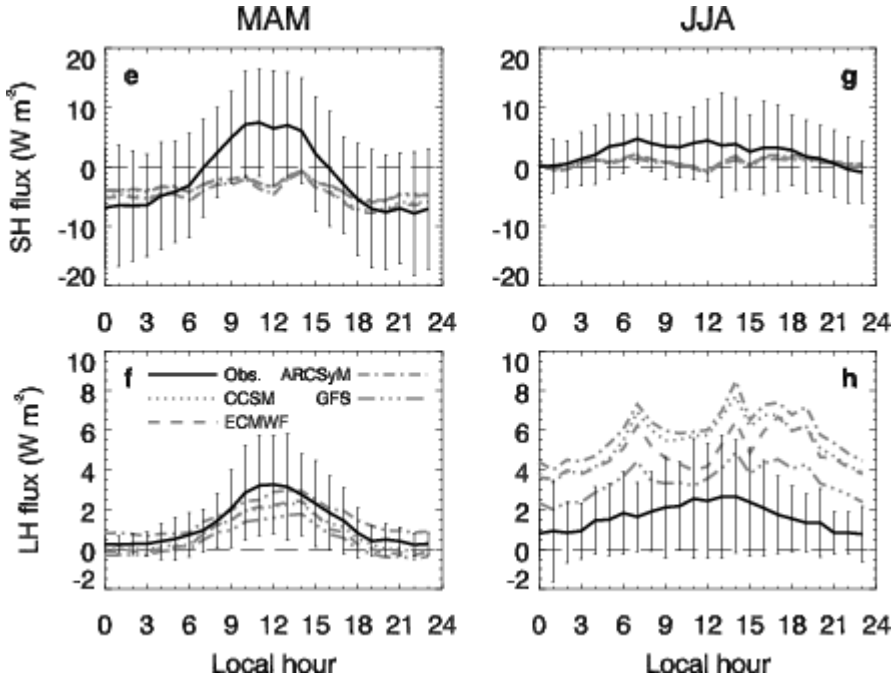

Figure 4 (cont'd).

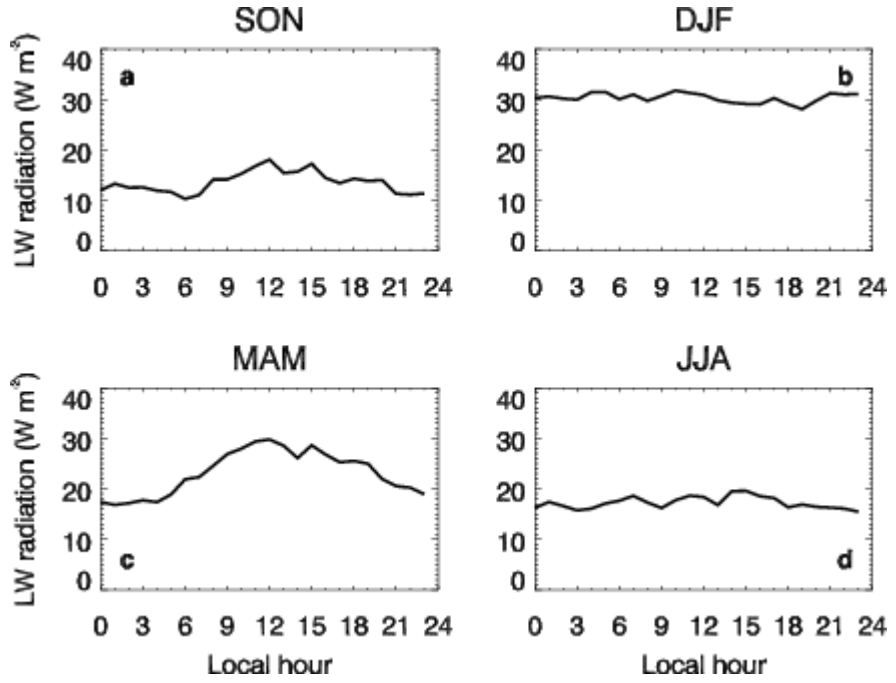

Figure 5. Hourly mean observed net longwave radiative fluxes at the 20-m tower in (a) SON, (b) DJF, (c) MAM, and (d) JJA. Positive fluxes are upward; negative fluxes are downward.

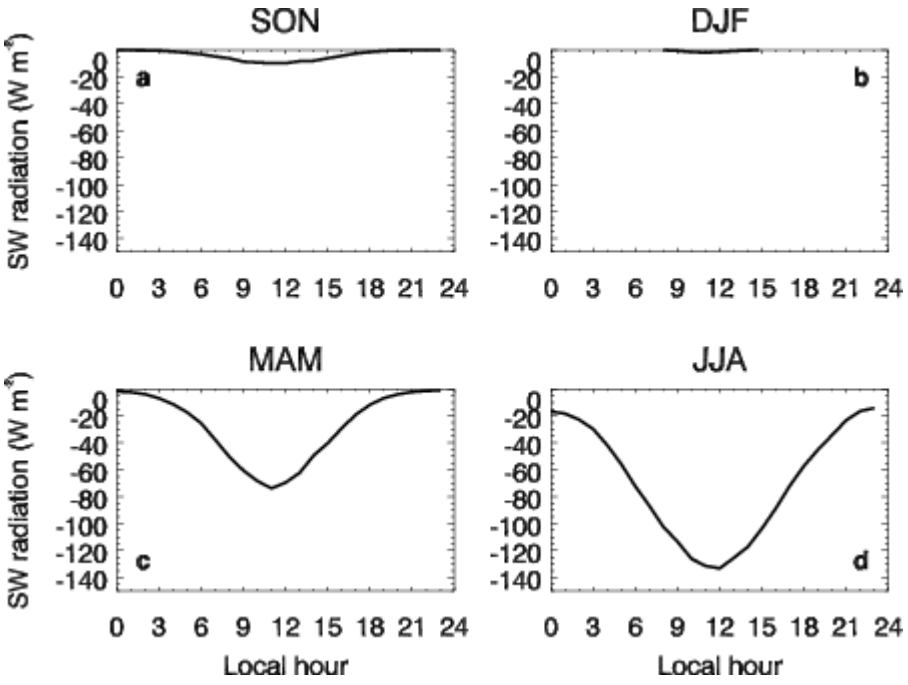

Figure 6. Same as in Figure 5 except for shortwave fluxes.

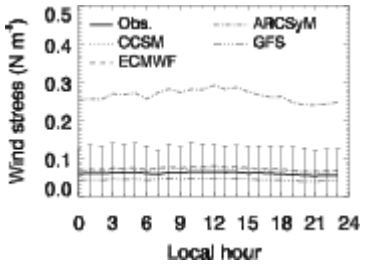

Figure 7. Hourly mean observed covariance wind stress along with the algorithm-produced fluxes from CCSM, ECMWF, ARCSyM, and GFS at the 20-m tower. The thin vertical lines represent one standard deviation about the mean.

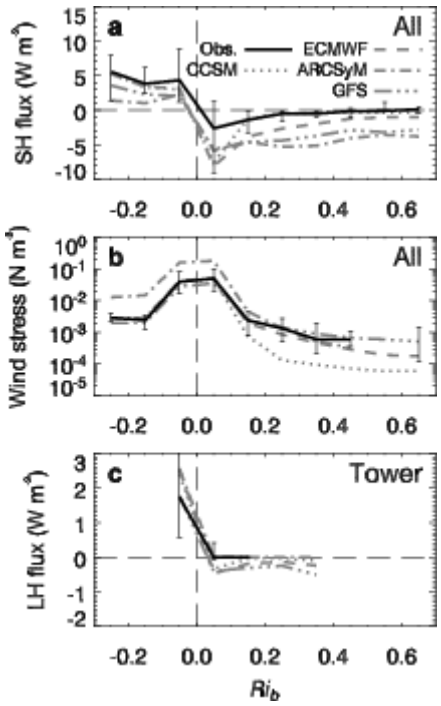

Figure 8. Median observed covariance (a) sensible heat fluxes, (b) wind stress, and (c) latent heat flux and the algorithm-produced fluxes from CCSM, ECMWF, ARCSyM, and GFS as a function of the bulk Richardson number Ri_b at 2.5 m in 0.1 bins for all of the four stations combined for (a,b) and for the 20-m tower for (c). The thin vertical lines represent the interquartile range, i.e., the difference between the 25th and 75th percentiles.

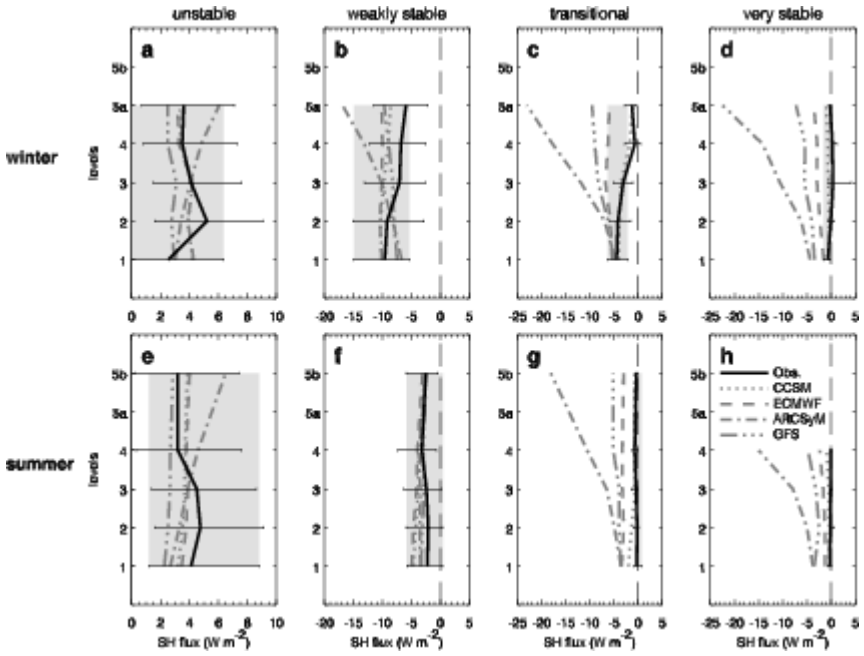

Figure 9. Median observed covariance sensible heat fluxes and the algorithm-produced fluxes from CCSM, ECMWF, ARCSyM, and GFS at each level of the 20-m tower for (a)-(d) winter (October to March) and (e)-(h) summer (April to September) in the (a,e) unstable ($Ri_b \leq 0$); (b,f) weakly stable ($0 < Ri_b \leq 0.05$); (c,g) transitional ($0.05 < Ri_b \leq 0.25$); and (d,h) very stable ($Ri_b > 0.25$) regimes. The thin horizontal lines represent the interquartile range, i.e., the difference between the 25th and 75th percentiles, and the shaded box shows the observed interquartile range at level 1.

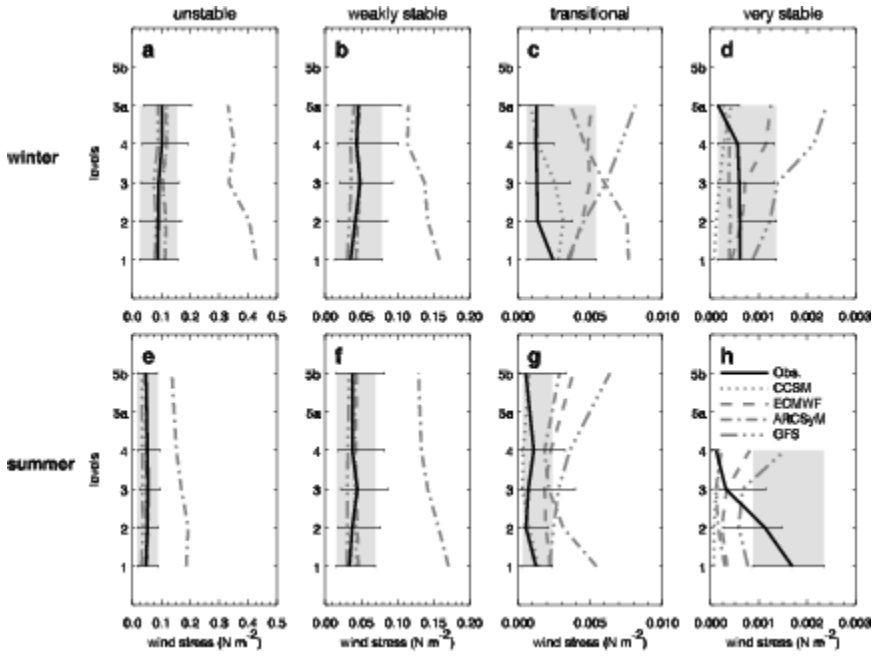

Figure 10. Same as in Figure 9 except for wind stress.

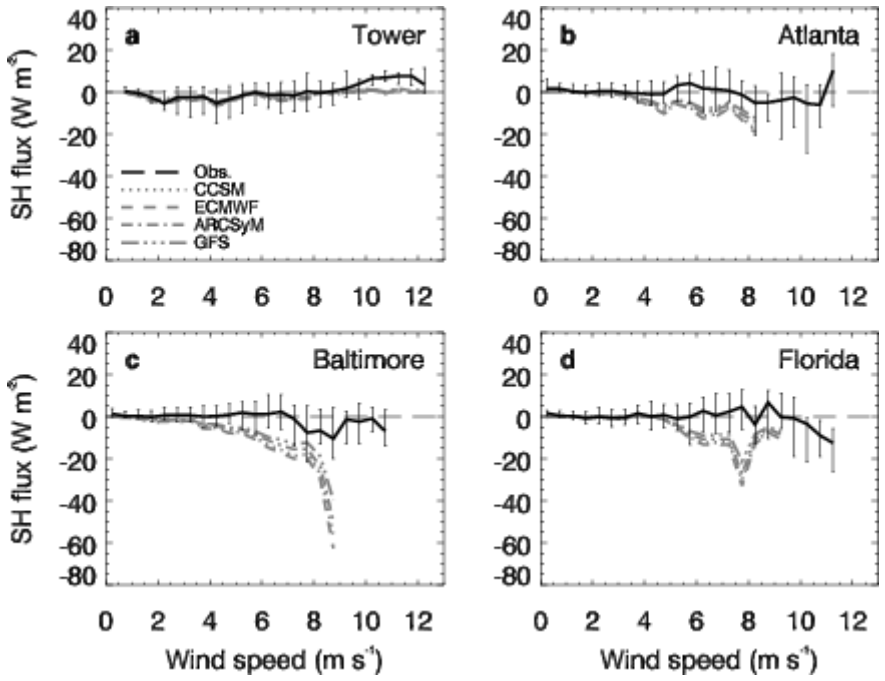

Figure 11. Median observed covariance sensible heat fluxes and the algorithm-produced fluxes from CCSM, ECMWF, ARCSyM, and GFS for 0.5 m s^{-1} bins of wind speed at 2.5 m at (a) the 20-m tower and the PAM stations (b) Atlanta, (c) Baltimore, and (d) Florida. The thin vertical lines represent the interquartile range, i.e., the difference between the 25th and 75th percentiles.

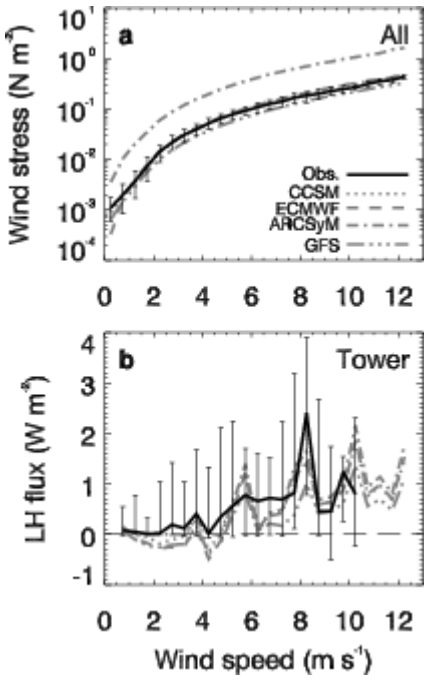

Figure 12. Median observed covariance (a) wind stress for all of the four stations combined and (b) latent heat fluxes at the 20-m tower and the algorithm-produced fluxes from CCSM, ECMWF, ARCSyM, and GFS for 0.5 m s^{-1} bins of wind speed at 2.5 m. The thin vertical lines represent the interquartile range, i.e., the difference between the 25th and 75th percentiles.

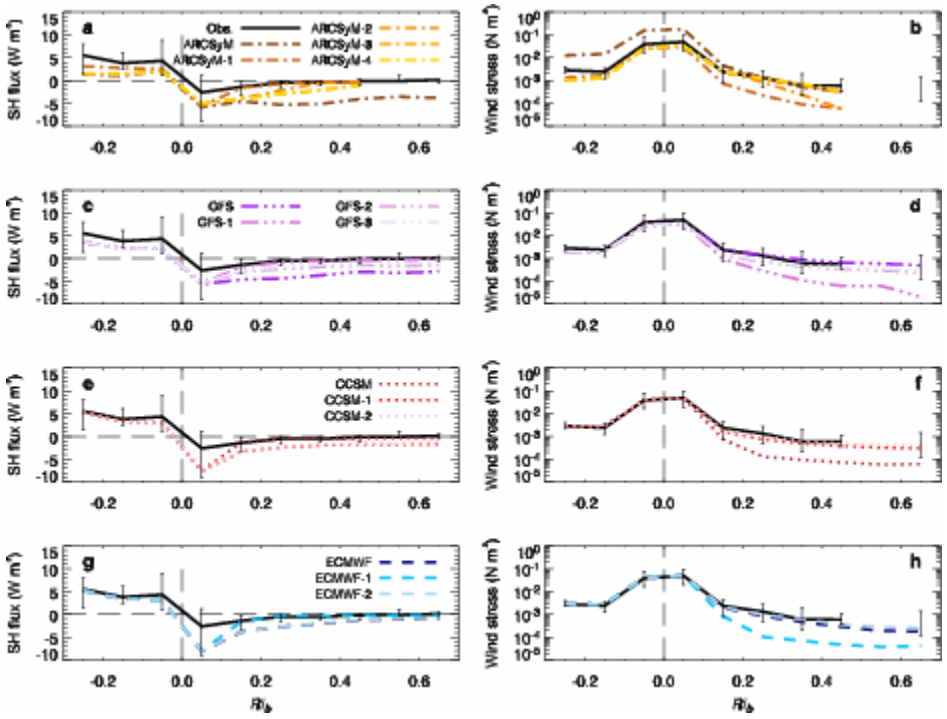

Figure 13. Median observed covariance (a,c,e,g) sensible heat fluxes and (b,d,f,h) wind stresses for all of the four stations combined. The thin vertical lines represent the interquartile range. Also plotted are the sensible heat fluxes calculated by (a,b) ARCSyM and its altered versions used in the sensitivity tests (ARCSyM-1, ARCSyM-2, ARCSyM-3, ARCSyM-4), GFS and its altered versions (GFS-1, GFS-2, GFS-3), CCSM and its altered versions (CCSM-1, CCSM-2), and ECMWF and its altered versions (ECMWF-1, ECMWF-2).

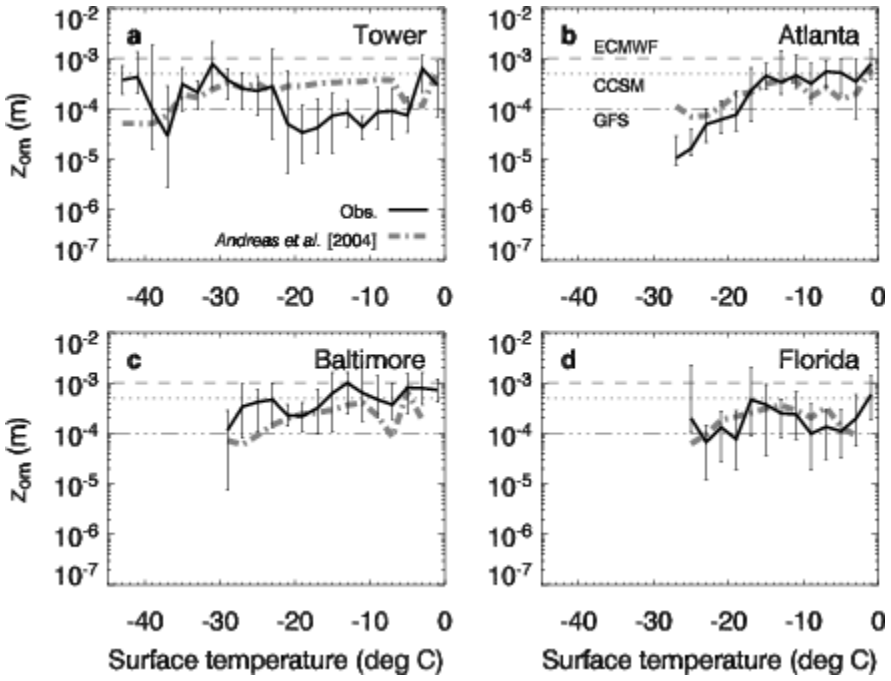

Figure 14. Median observed roughness lengths for momentum (z_{om}) for 2°C bins of surface temperature at (a) the 20-m tower and the PAM stations (b) Atlanta, (c) Baltimore, and (d) Florida. The thin vertical lines represent the interquartile range. Also shown are the roughness lengths from the *Andreas et al.* [2004] scheme as well as those used in ECMWF, CCSM, and GFS.

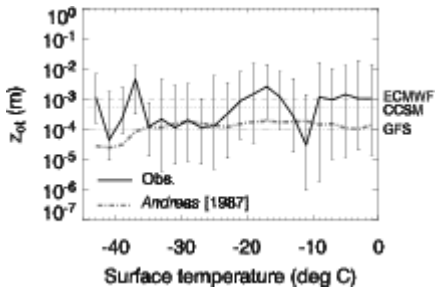

Figure 15. Median observed roughness lengths for heat (z_{ot}) for 2°C bins of surface temperature for all of the four stations combined. The thin vertical lines represent the interquartile range. Also shown are the roughness lengths from the *Andreas* [1987] scheme as well as those used in ECMWF, CCSM, and GFS.

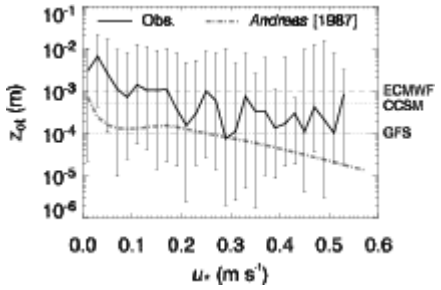

Figure 16. Median observed z_{ot} for 0.02 m s^{-1} bins of friction velocity u_* for all of the four stations combined. The thin vertical lines represent the interquartile range. Also shown are the roughness lengths from the *Andreas* [1987] scheme as well as those used in ECMWF, CCSM, and GFS.

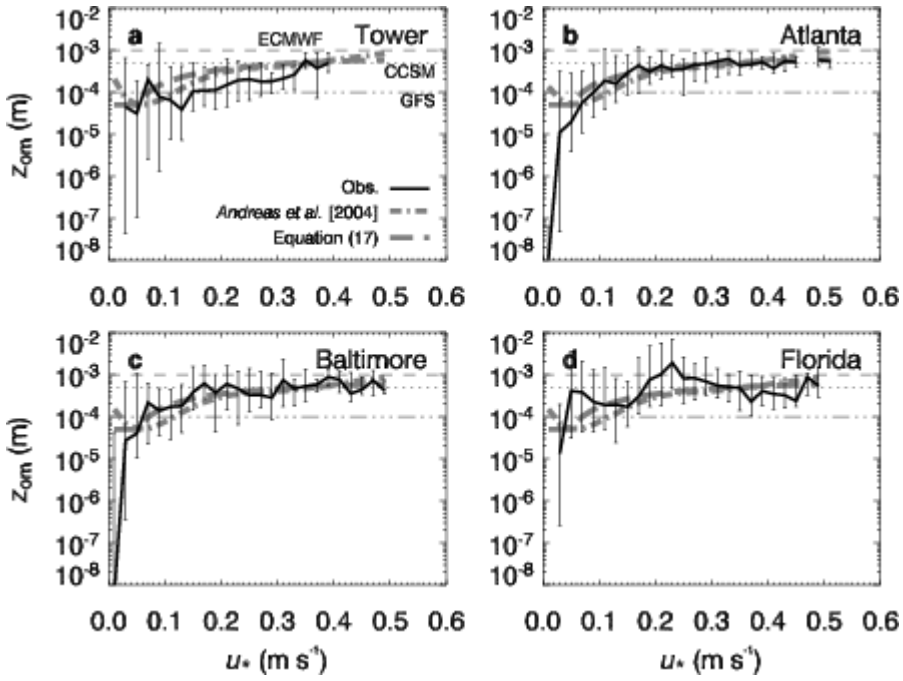

Figure 17. Median observed z_{om} for 0.02 m s^{-1} bins of friction velocity u_* at (a) the 20-m tower and the PAM stations (b) Atlanta, (c) Baltimore, and (d) Florida during the winter aerodynamically speaking (before 15 May 1998 and after 14 September 1998). The thin vertical lines represent the interquartile range. Also shown are the median roughness lengths derived from equation (17) as well as those from the *Andreas et al.* [2004] scheme and those used in ECMWF, CCSM, and GFS.

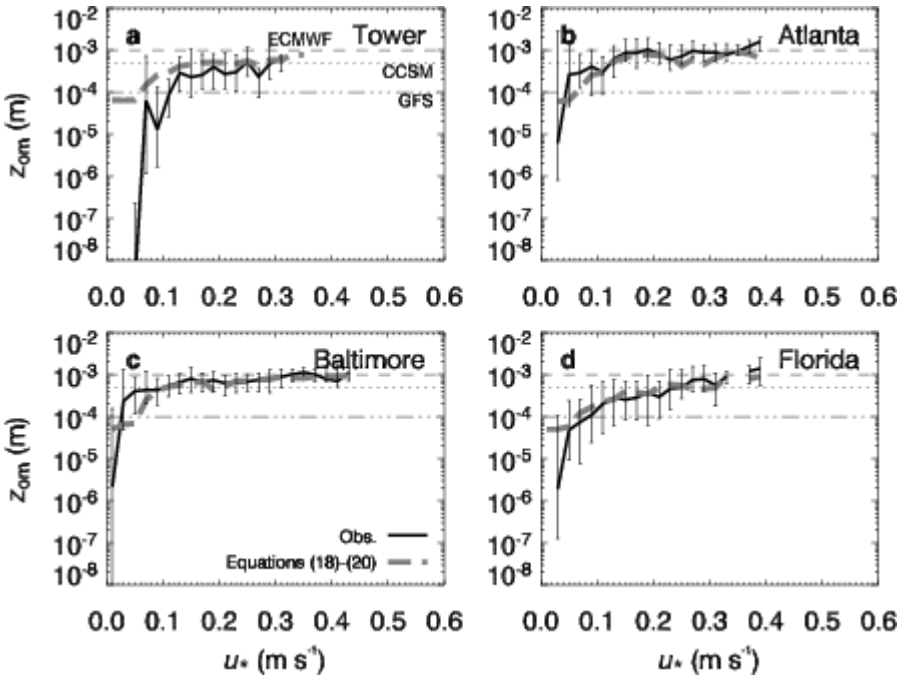

Figure 18. Same as in Figure 17 except for aerodynamic summer. Also shown are the median roughness lengths from equations (18)-(20).